Quaternary Science Reviews 344 (2024) 108948

Contents lists available at ScienceDirect

Quaternary Science Reviews

journal homepage: www.elsevier.com/locate/quascirev

Disentangling seasonal and annual precipitation signals in the tropics over the Holocene: Insights from δD, alkanes and GDGTs

Petter L. Hällberg [a,*], Rienk Smittenberg [a,b], Malin E. Kylander [a], Joan Villanueva [c], Nina Davtian [c], Anggi Hapsari [d], Jenny K. Sjöström [a,e], Josefine Axelsson [e], Guillermo Jarne-Bueno [a], Kweku Yamoah [f], Hamdi Rifai [g], Frederik Schenk [a,h]

[a] Bolin Centre for Climate Research and Department of Geological Sciences, Stockholm University, Svante Arrhenius väg 8C, 10691, Stockholm, Sweden
[b] Swiss Federal Institute for Forest, Snow and Landscape Research WSL, Birmensdorf, Switzerland
[c] Institute of Environmental Science and Technology, Universitat Autònoma de Barcelona (ICTA-UAB), Barcelona, Spain
[d] Albrecht-von-Haller Institute, University of Göttingen, Göttingen, Germany
[e] Department of Physical Geography, Stockholm University, Stockholm, Sweden
[f] Department of Archaeology, University of York, York, United Kingdom
[g] Department of Physics Faculty of Mathematics and Natural Sciences, Universitas Negeri Padang, West Sumatra, Indonesia
[h] Department of Geosciences and Geography, University of Helsinki, Helsinki, Finland

A R T I C L E I N F O

Handling Editor: P Rioual

Keywords:
Leaf waxes
Indo-Pacific warm pool (IPWP)
Southeast Asia
Biomarkers
Stable isotopes
Organic geochemistry
Paleoclimatology

A B S T R A C T

Rainfall seasonality in the tropics has a substantial impact on both ecosystems and human livelihoods. Yet, reconstructions of past rainfall variability have so far generally been unable to differentiate between annual and seasonal precipitation changes. Past variations in seasonality are therefore largely unknown. Here, we disentangle hydrogen isotopic (δD) signals from terrestrial leaf waxes and algae in an 8000-year peat core from Sumatra, which reflect annual versus wet season rainfall signals, respectively. We validate these results using lipid biomarkers by reconstructing vegetation dynamics via *n*-alkane distributions and peatland hydrological conditions using glycerol dialkyl glycerol tetraethers (GDGTs), as well as biomass burning using levoglucosan concentrations in the core. Finally, we compare our proxy results to a transient climate model simulation (MPI-ESM1.2) to identify the mechanism for seasonality changes. We find that algal δD indicates stronger Indonesian-Australian Summer Monsoon (IASM) precipitation in the Mid-Holocene, between 8 and 4.2 cal ka BP. A period of alternating flooding, droughts and wildfires is reconstructed between 6 and 4.2 cal ka BP, implicating very strong monsoonal precipitation and drying out and burning during a longer and intensified dry season. We attribute this strong rainfall seasonality in the Mid-Holocene mainly to orbitally forced insolation seasonality and a strengthened IASM, consistent with the modeling results. In terms of annual rainfall, terrestrial plant δD, vegetation composition and GDGTs all indicate wetter conditions peaking between 3 and 4.5 cal ka BP, preceded by drier conditions, followed by drastic and rapid drying in the late Holocene from around 2.8 cal ka BP. Our multiproxy annual precipitation reconstruction thereby indicates the wettest overall conditions approximately 1500–2000 years later than a nearby speleothem $\delta^{18}O$ record, which instead follows the seasonally biased algal δD in our record. We, therefore, hypothesize that speleothem reconstructions over the Holocene in parts of the tropics with low but significant seasonality may carry a stronger seasonal component than previously suggested. The data presented here contribute with new insights on how isotopic rainfall proxies in the tropics can be interpreted. Our findings resolve the seasonal versus annual components of Holocene rainfall variability in the Indo-Pacific Warm Pool region, highlighting the importance of considering seasonality in rainfall reconstructions.

* Corresponding author.
E-mail address: petter.hallberg@geo.su.se (P.L. Hällberg).

https://doi.org/10.1016/j.quascirev.2024.108948
Received 5 April 2024; Received in revised form 4 September 2024; Accepted 4 September 2024
Available online 4 October 2024

1. Introduction

Precipitation seasonality is a key aspect of climate and ecosystem dynamics in the tropics. Whether rainfall is evenly distributed throughout the year or concentrated into a brief rainy season followed by a dry season can determine the development of rainforest or savanna ecosystems (Beck et al., 2018). Additionally, a more seasonal climate increases vulnerability to flooding, droughts and fire events, with significant implications for human livelihoods and food security. Assessing the drivers of seasonality in the tropics is therefore fundamental to understanding how the climate system will respond to current and future climate changes.

The Indo-Pacific Warm Pool (IPWP) region exports immense amounts of heat and moisture to the extratropics, making climate dynamics in the IPWP a major influence on the seasonal precipitation of the monsoons in both hemispheres (De Deckker, 2016). To date, research on past precipitation in the IPWP relied mainly on the water derived oxygen and hydrogen isotopic signature recorded in speleothems ($\delta^{18}O_{speleo}$) and fossil leaf waxes (δD_{wax}) in sediment records. The water isotopic composition of precipitation in the IPWP is strongly influenced by the regional convective strength and the associated 'amount effect' (Kurita et al., 2009), and rainfall amount has therefore been the main interpretation of water isotopic records (Cobb et al., 2007; Dansgaard, 1964). However, water isotopes in precipitation are also dependent on moisture source, rain out trajectory and short term climate events such as the El Niño Southern Oscillation (ENSO) and the Madden-Julien Oscillation, thus complicating the interpretation of the isotope records (Belgaman et al., 2017; Konecky et al., 2016; Yuan et al., 2023). The effect of changes in seasonality through time has not received enough attention in the proxy interpretation of water isotope dynamics, and the focus has mostly been on the 'amount effect' recorded by the isotopic proxies. However, whether the precipitation 'amount' reflects the wet season or annually integrated rainfall amounts has been challenging to quantify, especially considering that hydrological drivers of rainwater $\delta D/\delta^{18}O$ ($\delta D_{rainwater}$ and $\delta^{18}O_{rainwater}$) for a specific site may vary over time (Wurtzel et al., 2018). As a result, past precipitation seasonality in this key region, in particular over the Holocene, needs to be further constrained, as it may have significant relevance for our understanding of past hydroclimate dynamics.

δD_{wax} is recorded by terrestrial plants which grow throughout the year in the tropics (Malhi et al., 2014a, 2014b) and therefore likely reflect an integrated annual water isotopic signal (Niedermeyer et al., 2014). However, some uncertainties remain; Konecky et al. (2016) hypothesized that if δD_{wax} records a seasonally biased signal, it would be biased towards the wet season via amount weighted isotopic mean composition of groundwater. In contrast, Feakins et al. (2016) suggested that tropical δD_{wax} may be biased towards the dry season, as waxes are preferentially produced during the leaf flushing, which mostly occurs during the drier, less cloudy season in their study area in the Amazon. Moreover, leaf evapotranspiration during drier periods may cause a distinct isotope enrichment of leaf waxes (Sachse et al., 2012). The current knowledge on the effects of seasonality on δD_{wax} is limited, and how seasonality affects δD_{wax} in downcore records in the IPWP remains unexplored.

In contrast to leaf waxes produced by plants, speleothem growth is tied to groundwater recharge (Lases-Hernandez et al., 2019; Moerman et al., 2013). Cave $\delta^{18}O_{speleo}$ is built up during carbonate precipitation from soil percolated drip water, which occurs mostly following wet season groundwater recharge (Baker et al., 2019; Clark and Fritz, 1997; Cobb et al., 2007; Dansgaard, 1964; Fairchild and McMillan, 2007; Lases-Hernandez et al., 2019; Qiu et al., 2023; Rozanski et al., 2013). Speleothem carbonate $\delta^{18}O$ may either be representative of amount weighted annual average $\delta^{18}O_{rainwater}$, or be biased towards the season with the highest carbonate depositional or groundwater recharge rates (Baker et al., 2019; Lachniet, 2009; Ridley et al., 2015). In the IPWP, Yuan et al. (2023) interpret speleothem $\delta^{18}O$ on Sulawesi and Sumatra to reflect an annually averaged signal, based on the similarity in trends on both islands. On the contrary, Wolf et al. (2023) and Ayliffe et al. (2013) exclusively interpret speleothem $\delta^{18}O$ as seasonal indicators, given that their study areas receive precipitation mainly during the wet season. Precipitation isotopes recorded at sites that receive precipitation over a large part of the year, such as Sumatra and Borneo may instead be driven by changes in the relative input from different moisture sources (Wurtzel et al., 2018; Partin et al., 2007), in addition to evaporation and selective recharge (Baker et al., 2019). For Sumatra, this leads to higher $\delta^{18}O$ during the boreal summer when precipitation is sourced from the southern hemisphere and lower $\delta^{18}O$ during the rest of the year. This effectively results in an enhanced amount effect on Sumatra, due to lower precipitation amounts during boreal summer, when a low amount of isotopically heavy precipitation is sourced from south of the equator (Wurtzel et al., 2018). Model-proxy comparison from Borneo shows that seasonal (winter) drying affected speleothem $\delta^{18}O$ during the Heinrich Stadial 1 and Younger Dryas events of the deglacial period (Buckingham et al., 2022). It is therefore clear that seasonal changes in precipitation can drive speleothem oxygen isotope variability. However, it remains difficult to disentangle the contribution from different seasons and it is unclear how isotopic precipitation records should be interpreted in terms of seasonality, in particular during the Holocene.

An advantage of isotopic reconstructions based on leaf waxes and other lipid biomarkers is that the isotopic composition from multiple compounds can be acquired from the same sample in a single measurement. In particular, this has been done on *n*-alkanes with chain lengths between 21 and 33 carbon atoms (C_{21} to C_{33}) where C_{21} to C_{25} have been reported to be produced by aquatic plants, and the longer chains $> C_{27}$ are produced by terrestrial plants (Aichner et al., 2010; Bush and McInerney, 2013; Ficken et al., 2000). These *n*-alkanes are a main component of protective epicuticular leaf waxes from plants. *n*-alkanes shorter than C_{21} are sourced mainly from algae and microbes (Aichner et al., 2010). The habitat and growth period of the different source organisms can be used to derive additional information on the drivers of their isotopic composition, including seasonal aspects of the hydroclimate. The isotopic signals of *n*-alkanes can therefore be used to reconstruct isotopic variability in a range of environments and hydrogen sources. For instance, Katrantsiotis et al., 2021 used the δD signals from terrestrial and aquatic plants (δD_{terr} and δD_{aq}) to derive different seasonal signals: an annually averaged lake water δD signal from the aquatic plants while the terrestrial plants reflected the summer precipitation δD, based on their different water sources. Similarly, the difference between δD_{terr} and δD_{aq} has been interpreted as a measure of soil evaporative enrichment, moisture availability and relative humidity (Muschitiello et al., 2015; Rach et al., 2014; Sachse et al., 2012). The isotopic signature of an organism growing during only a short period of the year can therefore yield information about water isotopes from that specific season. In contrast, plants that either grow over the whole year, or derive their water from a source that has accumulated over a longer time period reflect a weighted average of incoming precipitation, modulated by potential evaporative enrichment during drier seasons with negative precipitation-evaporation balance (Thomas et al., 2020).

In this study, we take advantage of the δD signals recorded by plants and algae that grow during – and record water isotope signals from – different periods of the year. We use a peat core from Sumatra that has been accumulating over the past 8000 years (Hällberg et al., 2023), with the goal of reconstructing past rainfall and seasonality. Terrestrial plants grow throughout the whole year in the tropics, while algae only grow during the wet season following peat flooding. In this way, we generate two δD records, one for the annual average and one for the wet season only, allowing disentanglement of the seasonal and annual rainfall signals. To validate these δD results, we use additional independent proxies that allow reconstruction of the hydrological conditions of the peatland. By assessing the distribution of alkanes C_{19}-C_{35}, we reconstruct the relative amounts of algae, aquatic plants and terrestrial plants, which

reflect peatland flooding and peat long term wetness. We also use the distribution of microbial membrane-derived glycerol dialkyl glycerol tetraethers (GDGTs), which can be used to reconstruct water table variations, droughts, and peat wetness (De Jonge et al., 2024). Furthermore, we present a record of past biomass burning, based on the concentration of levoglucosan, an anhydrosugar produced upon cellulose burning (Suciu et al., 2019). We then explore the mechanisms for changes in past seasonality using a transient climate model simulation. Lastly, we discuss the implications of our results for how isotopic precipitation reconstructions may be interpreted in the region. Based on this multi-proxy and modeling approach, we generate a robust rainfall/wetness reconstruction of Sumatra over the Holocene, and disentangle the seasonal and annual precipitation signals.

2. Materials and methods

2.1. Study area

The Padang wetland (2.206732°S, 101.526774°E) is situated at 959 m a.s.l. in the Kerinci Valley in western-central Sumatra in the province of Jambi. The wetland is a 0.8 km^2 valley bog, with a 5 ha (0.05 km^2) body of open water. Intense human activity is apparent around the wetland, with increasing amounts of surrounding forest being converted into farmland. At the time of sampling the site was covered by herbaceous swamp vegetation, dominated by macrophyte sedge *Machaerina rubiginosa,* with presence of woody plants and shrubs, including *Melastoma malabathricum* and *Ilex cymosa* (Morley, 1982). Based on pollen evidence, the undisturbed vegetation around the site evolved from herbaceous dominated marsh prior to swamp forest around 9000 years ago, while the vegetation similar to that of the 20th century developed around 7500 years ago (Morley, 1982). The bedrock in the area is volcanic, made up of intermediate to mafic rocks (Morley, 1982).

The current climate is wet and warm throughout the year, with 3100 mm of precipitation falling annually according to the ERA5 dataset between 1979 and 2020 CE (Fig. 1) (Hersbach et al., 2020). The boreal autumn-winter months are the wettest, particularly November, due to the seasonal migration of the intertropical convergence zone (ITCZ). Likewise, greater amounts of precipitation fall during the early boreal spring (March and April) and also during the migration of the ITCZ. The monsoon season around November is associated with rainfall sources from the north and west, i.e., the Asian Winter Monsoon and the Indonesian-Australian Summer Monsoon (IASM). June is the driest month, associated with the onset of the Asian Summer Monsoon, or the Indonesian-Australian Winter Monsoon (IAWM) in the southern hemisphere (Wurtzel et al., 2018). During large parts of the year, moisture is primarily sourced from the Indian Ocean, when the ITCZ is over Sumatra in autumn and spring (Wurtzel et al., 2018). During the IASM, moisture is increasingly sourced from the South China Sea to the northeast. For the IAWM, moisture is sourced from the southern hemisphere, including the Indian Ocean, the Java Sea and the Timor Sea (Wurtzel et al., 2018). The water isotopes of precipitation roughly follow the same pattern as the amount of precipitation in Sumatra. Water δD and $\delta^{18}O$ are more negative during the wet periods associated with ITCZ precipitation and less negative, in particular during August and, to some extent, in February (Fig. 1) (Belgaman et al., 2017; Kurita et al., 2009; Wurtzel et al., 2018).

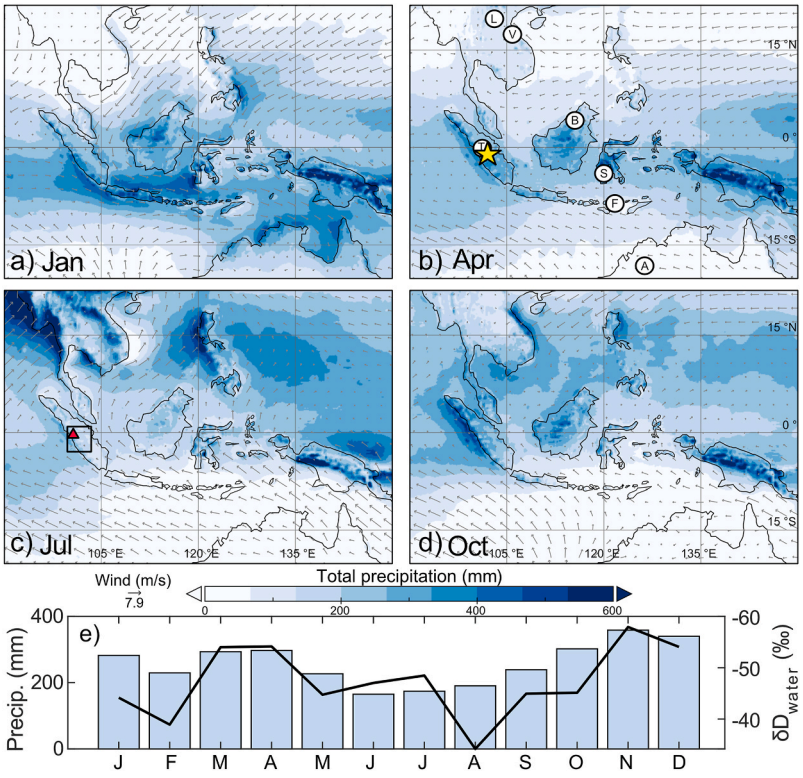

Fig. 1. Present day precipitation and wind patterns in January (a), April (b), July (c) and October (d) and monthly variability in water isotopic composition (e). The star in (b) marks the Padang peatland, and the labeled circles denote speleothem records from L: Laos, B: Borneo, T: Tangga Cave, F: Flores and A: Australia (Denniston et al., 2013; Griffiths et al., 2013, 2020; Partin et al., 2007). Precipitation and wind data are derived from ERA5 reanalysis data between 1979 and 2020 CE. The data in (d) for precipitation amount is ERA5 data from central Sumatra land areas (box between 1°N and 3°S and 100-104°E in (c)). The isotopic data is based on JAMSTEC measurements at the GAW/Kototabang station (red triangle in (c)) in Sumatra between 2001 and 2008 (Kurita et al., 2009). The line plot represents $\delta D_{rainwater}$, and the bars represent rainfall amounts in (e).(For interpretation of the references to colour in this figure legend, the reader is referred to the web version of this article.)

2.2. Sampling and radiocarbon dating

A 610 cm peat core was collected in March 2018 using a D-corer with a 50 × 6 cm chamber, retrieved from two alternating bore holes approximately 2 m apart, with a 10 cm vertical overlap. The cores were stored at 4 °C at NTU Singapore after sampling, from which an L-channel core was taken to Stockholm University, where the core was subsampled at 10 cm resolution in 1 cm slices, which were subsequently freeze-dried before analysis. Radiocarbon dating was conducted on 9 bulk samples from the Padang peat sequence at the Laboratory of Ion Beam Physics, ETH Zurich (Supplementary Table 1, Fig. 2). An age-depth model was constructed using *rbacon* version 3.1.1 (Blaauw and Christen, 2011) , and the SHCal20 calibration curve (Hogg et al., 2020).

2.3. Bulk elemental and isotope analysis

Total organic carbon (TOC) and carbon stable isotope ratios were measured at the Geological Institute, ETH Zurich, using a Flash-EA 1112 Elemental Analyzer (ThermoFischer Scientific) coupled to an isotope ratio mass spectrometer (Delta V, ThermoFisher Scientific) (EA-IRMS). TOC is reported in percent dry weight, and the isotope ratio is expressed as $\delta^{13}C$ in permille relative to VPDB.

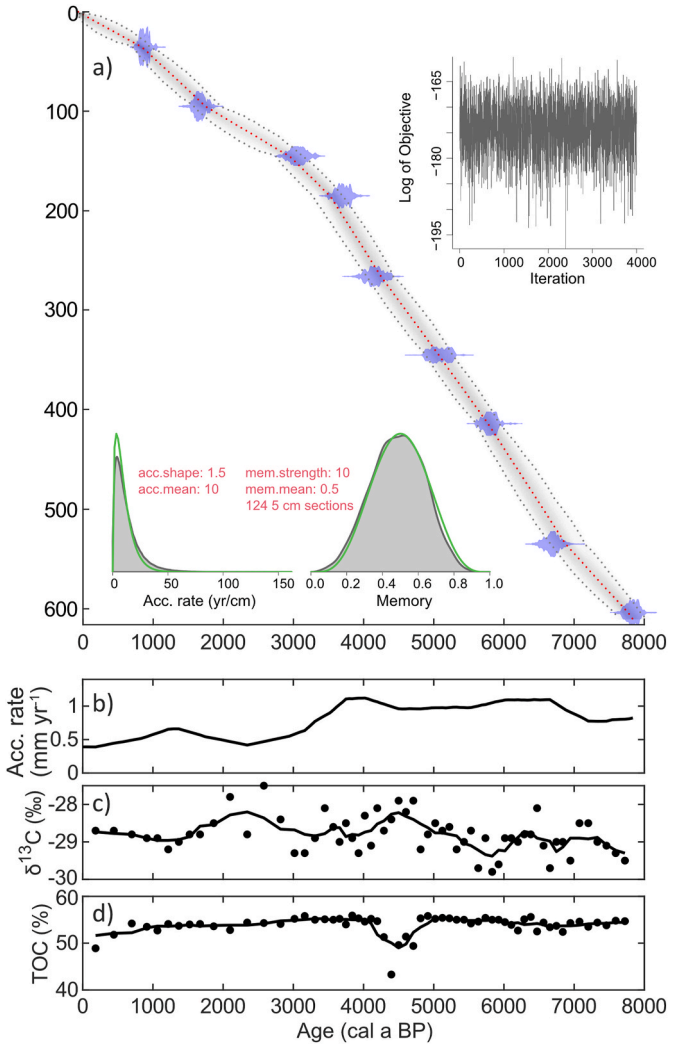

Fig. 2. Age model (a), peat accumulation rate (b), TOC (c) and bulk $\delta^{13}C$ (d) from the Padang peat sequence. The line plots are smoothed to a 50 cm running mean in (b) and to a 5-point running mean in (c) and (d). The upper inset in a) shows the Markov Chain Monte Carlo iterations and the lower insets in a) show the prior (lines) and posterior densities (area fills) for the mean accumulation rate and memory, respectively.

2.4. Lipid organic geochemistry

2.4.1. Extraction

Approximately 0.3 g dry weight of each sample was extracted using 20 ml Dichloromethane:Methanol (DCM:MeOH) 9:1 v/v mixture in an ultrasonic bath for 15 min after suspension using a vortex. Samples were then centrifuged at 800 rcf for 10 min. Since purely organic peat samples have a very low bulk density, particles and solvents did not fully separate in the DCM:MeOH mixture, and some hexane (which is a solvent with relatively low density) was added to those samples prior to centrifuging to allow sedimentation. The total lipid extract (TLE) was then transferred to a new vial, and the process was repeated three times. The TLE was then gently dried under a slow stream of N_2 on a 30 °C warming block. The N_2 flow was set very low in order to avoid evaporation of short alkanes which are relatively volatile. The TLE was redissolved in <1 ml DCM and adsorbed to pre-combusted deactivated (400 °C overnight, and after cooling down an addition of 5% H_2O) 95% silica gel. For fractionation of the TLE into apolar and polar fractions, the adsorbed samples were placed on silica gel pipette columns and eluted using three column volumes of hexane (apolar fraction, contained the *n*-alkanes) and DCM:MeOH (polar fraction, containing GDGTs). The apolar fraction was dissolved in hexane, and the polar fraction was dissolved in a mixture of hexane – isopropanol (99:1 v/v) and filtered through a 0.45 μm PTFE filter to remove poorly dissolved polar material prior to analysis.

2.4.2. GDGTs

GDGTs in Sumatra and in the Padang peat core have been discussed in depth by Hällberg et al. (2023), who focused on branched GDGT provenance and GDGT temperature reconstructions. Here, we focus on the hydrological interpretation of GDGTs.

GDGTs were analyzed using the method described by Hopmans et al. (2016) on 60 samples using a Dionex/Thermo Scientific UltiMate3000 high-performance liquid chromatograph equipped with two Waters Acquity UHPLC BEH HILIC columns (2.1 × 150 mm, 1.7 mm) connected to a TSQ Quantum Access Max Triple Quadrupole mass spectrometer (HPLC-MS) and APCI ion source in positive mode. A flow of 0.3 ml min^{-1} was used, as previously described by Hällberg et al. (2023). The mass spectrometer scanned at *m/z* windows centered around 1020 (scan width 7.5), 1034 (width 7.5), 1048 (width 7.5), and 1297 (width 15). The GDGTs were quantified manually using Xcalibur with a limit of quantification set to signal-to-noise ratio of >3. For further introduction to GDGTs and their annotation, we refer to Hällberg et al. (2023).

Although GDGT distributions in peats and soils are primarily driven by temperature and pH, other soil chemical parameters also influence their distribution, including oxygen availability and humidity (De Jonge et al., 2014). To calibrate GDGT distributions to peat pH, we calculated the cyclization of branched tetraethers index (CBT') (Eq. (1)) and used the transfer function (Eq. (2)) to derive the peat pH (De Jonge et al., 2014).

$$CBT' = \log \frac{Ic + IIa' + IIb' + IIIa' + IIIb'}{Ia + IIa + IIIa} \quad (1)$$

$$pH = 7.15 + 1.59 * CBT' \quad (2)$$

De Jonge et al. (2024) found a strong correlation between the distribution of isoprenoidal GDGTs and the mean monthly precipitation amount. The P_{GDGT} (Eq. (3)) index was proposed as a qualitative mean monthly precipitation proxy, where higher values indicate wetter conditions.

$$P_{GDGT} = \frac{GDGT1 + GDGT3}{GDGT1 + Crenarchaeol} \quad (3)$$

The fact that certain GDGTs are predominantly produced by

methanogenic archaea has been used as an indication for the presence of methanogens and thereby anoxic conditions, which resulted in the Methane Index (Eq. (4), where cren is short for crenarchaeol) (Zhang et al., 2011) which is similar – but not identical – to P_{GDGT} in that it is driven by the crenarchaeol fractional abundance compared to some of the other GDGTs. The underlying mechanism for these proxies is that crenarchaeol is indicative of oxygenated conditions that are required for ammonium oxidation by their source organisms. P_{GDGT} is further driven by a correlation of GDGT3 with precipitation (De Jonge et al., 2024). In this study, we also explore the reverse approach, instead of using the methane index to indicate anoxic conditions (which is a near-permanent condition in peats), we use the fractional abundance of crenarchaeol, defined as the relative abundance of crenarchaeol compared to all analyzed isoprenoidal GDGTs, as a proxy for oxygenated conditions (Hällberg et al., 2023 and references therein).

$$Methane\ index = \frac{GDGT1 + GDGT2 + GDGT3}{GDGT1 + GDGT2 + GDGT3 + Cren + Cren\ isomer} \quad (4)$$

2.4.3. Alkane concentrations

n-alkanes (C_{19}-C_{35}) were quantified by gas chromatography-mass spectrometry (GC–MS) on a Shimadzu GCMS-QP2010 Ultra, equipped with an AOC- 20i autosampler and a split-splitless injector operated in splitless mode. A Zebron ZB-5HT Inferno GC column (30 m × 0.25 mm x 0.25 μm) was used for separation. The GC oven temperature was programmed from 60 to 180 °C at a rate of 20 °C min^{-1} and then ramped to 320 °C at a rate of 4 °C min^{-1} with a hold time of 20 min. MS operating conditions were set to an ion source temperature of 200 °C and 70 eV ionization energy. The apolar fraction was dissolved in 1000 μL hexane, and injection volumes were 1 μL. Spectra were collected using GC solution Workstation software (v2). Quantification was performed on odd-numbered alkanes C_{19}-C_{35} by using a calibration curve generated using a standard mixture with C_{13}-C_{40} alkanes forced through zero. Alkanes shorter than C_{19} or longer than C_{35} were consistently below the limit of quantification and were not included in this study. Replicate analyses (n = 12) of the external standard showed that the standard deviation in the commonly used indexes ACL, Paq, C_{33}/C_{29} (Diefendorf and Freimuth, 2017) and fractional abundance of C_{19} (eq. (5)) were 0.12, 0.01, 0.03 and 0.01, respectively. To explore alkane chain lengths covariation, principal component analysis (PCA) was conducted on the normalized alkane distributions using JMP Pro v16 (JMP, 2021). Alkane concentrations are expressed as ng g^{-1} of dry sediment.

The fractional amount of C_{19} compared to longer chains was calculated as the relative concentration of C_{19} compared to odd-chain alkane concentrations (Eq. (5)). C_{19} has previously been found to be sourced mainly from algae and bacteria (Sachse et al., 2004).

$$f(C_{19}) = \frac{C_{19}}{C_{19} + C_{21} + C_{23} + C_{25} + C_{27} + C_{29} + C_{31} + C_{33} + C_{35}} \quad (5)$$

The amount of mid-length *n*-alkanes was calculated as C_{21} to C_{27} relative to all odd-chain length alkanes ($f(C_{21}$-$C_{27})$, Eq. (6)). This is similar to the widely used P_{aq} index, which is used as a proxy for aquatic plants and is based on C_{23} and C_{25} (Aichner et al., 2010; Ficken et al., 2000). Here we use the wider version which includes C_{21} and C_{27}, based on our PCA results (Section 3.3) which show grouping and therefore likely similar source vegetation and/or environmental drivers of all chain lengths C_{21} to C_{27}.

$$f(C_{21} - C_{27}) = \frac{C_{21} + C_{23} + C_{25} + C_{27}}{C_{19} + C_{21} + C_{23} + C_{25} + C_{27} + C_{29} + C_{31} + C_{33} + C_{35}} \quad (6)$$

To quantify the relative abundance of the longer *n*-alkanes, which are mostly sourced from terrestrial plants (Aichner et al., 2010), we calculated the $f(C_{29}$-$C_{33})$ index based on the relative abundance of C_{29}-C_{33} relative to all odd-chain alkanes (Eq. (7)).

$$f(C_{29} - C_{33}) = \frac{C_{29} + C_{31} + C_{33}}{C_{19} + C_{21} + C_{23} + C_{25} + C_{27} + C_{29} + C_{31} + C_{33} + C_{35}} \quad (7)$$

2.4.4. Leaf wax δD

The hydrogen isotopic composition of odd-numbered alkanes C_{19} to C_{33}, was determined by gas chromatography-pyrolysis-isotope ratio monitoring-mass spectrometry (GC-IRMS) with a Thermo Finnigan Delta V plus mass spectrometer interfaced with a Trace Ultra GC, GC Isolink and Conflo IV interface, as described earlier (Norström et al., 2018). A standard mixture of alkanes with known isotopic composition (reference mixture A6, provided by Arndt Schimmelmann, Indiana University, USA) was run several times daily to calibrate the reference gas against which the samples were measured. Only peaks larger than 5 Vs were integrated, since repeat measurements showed that peaks <5 Vs had increased standard deviation in values. Most data points are based on the average of two to three measurements and results are reported as the mean in standard delta notation (δD) against VSMOV. For low-intensity peaks, data points were often derived from fewer measurements, and some chain lengths were not measured in samples where they had too low concentrations. More precisely, the average number of measurements was 2.4, 1.5, 1.7, 2.5, 2.5, 3.0, 3.0, and 2.7 for alkanes C_{19}, C_{21}, C_{23}, C_{25}, C_{27}, C_{29}, C_{31} and C_{33} homologs, respectively. The average standard deviation in isotopic values between replicate measurements was 3.1, 4.7, 4.2, 3.5, 2.2, 1.7, 1.7 and 4.2 ‰ for C_{19}, C_{21}, C_{23}, C_{25}, C_{27}, C_{29}, C_{31} and C_{33}, respectively, i.e., generally smaller errors for high abundance alkanes. We calculated the δD signal from terrestrial plants (δD_{terr}) as the average of δD_{C29} and δD_{C31} since C_{29} and C_{31} alkanes had the highest concentrations and therefore provided the most robust results.

2.5. Biomass burning biomarkers

The monosaccharide anhydrides (MAs) levoglucosan, galactosan, and mannosan are extensively used as selective tracers of fire-derived organic matter in the environment (Marynowski and Simoneit, 2022). A selected number of samples (n = 15) was analyzed for MAs at the Universitat Autònoma de Barcelona using the method described in detail by Davtian et al. (2023). In short, 0.2 g of freeze dried and powdered samples taken from 3 cm long core slices were extracted by automated solvent extraction (ASE), first using a mixture of hexane and acetone (1:1) to remove lipidic compounds, and subsequently using MeOH to obtain extracts containing the MAs. A known amount of internal standard (IS) ($^{13}C_6$-levoglucosan) was added before extraction for quantification. After concentration to dryness under a N_2 flow, the extracts were purified using ligand exchange SPE with Amberchrom 50WX8 resin in sodium form. After rinsing with DCM/MeOH (9:1 v/v), the MAs were eluted with MeOH and MilliQ H_2O. The purified fractions were desalted using Amberlite MB20 mixed-bed ion exchange resin and collected in 50 mL polypropylene tubes. Sample extracts were dried under N_2 and reconstituted in polypropylene vials after filtration using 0.45 μm PTFE filters. LC-MS/MS analysis was performed on a modular HPLC system (Agilent 1290 Infinity with quaternary pump) coupled to a triple quadrupole detector (Agilent 6470 LC/TQ) using electrospray ionization (ESI). Separation was achieved with a Se-Quant ZIC-HILIC (150 × 2.1 mm, 3.5 μm particle size, Merck) column maintained at 20 °C, with a mobile phase gradient (flow rate 0.275 ml min^{-1}) consisting of MilliQ H_2O (A) and acetonitrile (B). Post-column addition of 0.1 ml min^{-1} of an NH_4OH solution was used to enhance the MS/MS signal. All MAs isomers were detected in negative mode using the *m/z* 161/101 MS/MS transition and the IS using *m/z* 167/105. MAs concentrations were calculated using the peak area ratios of the analyte and the IS, and against a calibration curve consisting of 7 standard solutions (1–1000 ng mL^{-1}, 10 mL injections). Data analysis was performed using MassHunter workstation software 10.0 SR1 (Agilent). The method used is robust, provides repeatable concentration values for the MAs irrespective of the sample matrix, and applies to a wide concentration range. More details, including linearity, sensitivity, and repeatability, are given in Davtian et al. (2023). No replicates analyses were performed except

for the sample from 0 to 3 cm, and the sample from 311 to 314 cm depth. The latter had a much higher concentration than the other samples, and the second analysis was therefore performed on an extract derived from 0.02 g of dry sediment to confirm the results of the first measurement. Based on other results from the laboratory, the analytical uncertainty is estimated to be 15% for levoglucosan and 30% for the other two MAs.

2.6. Climate model simulation

To investigate the underlying mechanisms responsible for climate variations recorded by the proxy data, we analyzed the transient climate model simulation MPI-ESM 1.2 (The Earth System Model of the Max Planck Institute for Meteorology) (Bader et al., 2020; Dallmeyer et al., 2021) for the past 8000 years. MPI-ESM 1.2 is a fully coupled (ocean – atmosphere – land) full-forcing (orbital forcing, greenhouse gases, with dynamic vegetation) at a resolution of 1.875° in the atmosphere and 1.5° in the ocean. The simulation is described in detail by Dallmeyer et al. (2021) and Bader et al. (2020).

When presented as time series, the model output data was derived from boxes with coordinates between 96 and 107 °E, 7 °S-3 °N and 100–125 °E, 5 °S-5 °N, representing Sumatra and the Maritime Continent, respectively.

3. Results

3.1. Lithology and age model

The Padang peat is mostly ombrotrophic with very little mineral input from surrounding soils and has a homogenous and unstratified fully organic peat texture of black-brown color throughout (Munsell color 10YR2/1, except the upper 26 cm which is slightly lighter at 7.5YR2.5/2). The result of the radiocarbon dating and age-depth modeling showed that the sequence has been accumulating since 7.78 cal ka BP (range of 8.03-7.63 cal ka BP at 610 cm depth) (Fig. 2) and that all dates occur in chronological order with depth. Based on the age-depth model and the 10 cm sample interval, the temporal resolution for our samples is approximately 100–200 years, with a 130-year average. The fastest accumulation rate occurred between 6.8 and 3.8 cal ka BP at ~1 mm year^{-1}. From ~3 cal ka BP until the present, the accumulation rate approximately halved to ~0.5 mm year^{-1}. The mean age uncertainty of the age model is ±225 years (range 3–336 years) at the 2σ (95 %) range (shaded area in Fig. 2a, calculated as max-min age estimate from the bacon age model). The $\delta^{13}C$ signal measured on bulk sediments was on average −28.8 ± 0.48 ‰ (Fig. 2) (n = 60, 1σ) (range −29.8 to −27.5 ‰). Within these changes, the period with the lowest values was near the base between 7.8 and 5.5 cal ka BP, followed by the highest values ~4.5 cal ka BP. TOC was stable throughout the core, averaging 52.9 ± 2 %, with a short period of lowered TOC between 4.8 and 4.3 cal ka BP. The minimum TOC was 43.3 % from sample depth 280 cm at 4.37 cal ka BP (Fig. 2).

3.2. GDGTs

We reconstructed the pH at the site, based on CBT' (De Jonge et al., 2014). The results indicate relatively acidic conditions in the accumulated deposit, and changes of less than one pH unit over the entire depositional period (Fig. 3). The most acidic conditions were reconstructed between 4.3 and 2.5 cal ka BP, peaking at pH ~4, after a gradual decrease of pH since the beginning of the record starting at pH ~4.7. The qualitative precipitation index based on GDGTs, P_{GDGT}, indicates a maximum in precipitation or wetness between 4.1 and 3.2 cal ka BP, and approximately the same wetness in the early and late parts of the record (De Jonge et al., 2024). Crenarchaeol, produced by ammonia-oxidizing archaea that require oxygen (Hällberg et al., 2023 and references therein), peaks between 5.8 and 4.3 cal ka BP and displays a second, increasing trend towards the surface. The methane index is indicative of methanogenic conditions (Zhang et al., 2011) and shows very high values throughout the core (Supplementary Fig. 1). The methane index and crenarchaeol abundance show similar but opposing trends, due to the fact that crenarchaeol is part of the denominator of the methane index.

3.3. Alkane distribution

The *n*-alkane concentrations are highest for the C_{29} and C_{31} homologs, followed by C_{27}, C_{33}, C_{19} and C_{25} (Fig. 4a). C_{21}, C_{23} and C_{35} exhibit low concentrations in most samples. The down-core variability in concentrations for all individual chain lengths is shown in Supplementary Fig. 2. A PCA was conducted on *n*-alkane concentrations in all samples. Principal components one (PC1) and two (PC2) explain 42.7 and 20.2 % of the dataset variability, respectively (Fig. 4). The PCA shows a clear grouping of the mid-chain alkanes (C_{21} to C_{27}), plotting positively on the PC1 axis and around 0 on the PC2 axis. The shortest alkane measured, C_{19}, plots similarly, but separately, from the C_{21}-C_{27} alkanes, positively on PC1 and negatively on PC2. The longer chain alkanes (C_{29} to C_{33}) all plot negatively on the PC1 axis, opposite to the mid and short chains, but they are separated on the PC2 axis. The longest alkane measured, C_{35}, plots uniquely as positive on both PC1 and PC2. *A posteriori* plotted variables in the PCA (i.e., are not included in the PCA calculation) show that high pH (derived from GDGTs, see Section 3.2) correlates with negative PC1 values and low pH is correlated with a high abundance of short and mid-length alkanes. δD_{terr} and P_{GDGT} (precipitation proxies, see Sections 3.2 and 3.4) plot positively on PC1 and slightly positively on PC2 axes, similar to the mid-chain n alkanes. $\delta^{13}C$ also plots positively on PC1, and slightly negatively on PC2 axes, similar to C_{19} and the mid-chain lengths.

Based on the groupings of the *n*-alkanes in the PCA and their trends, we calculated a mid-chain fractional abundance ($f(C_{21}$-$C_{27})$) for C_{21} to C_{27} homologs, $f(C_{29}$-$C_{33})$ based on C_{29} to C_{33}, and $f(C_{19})$ for the C_{19} *n*-alkane (see Methods) (Fig. 5). $f(C_{19})$ peaked between 6 and 4 cal ka BP. The $f(C_{21}$-$C_{27})$ shows a gradual increase with a later maximum around 3.5 cal ka BP, and a subsequent decrease towards the present. The long-chain *n*-alkanes exhibit an almost opposite behavior to mid-chain

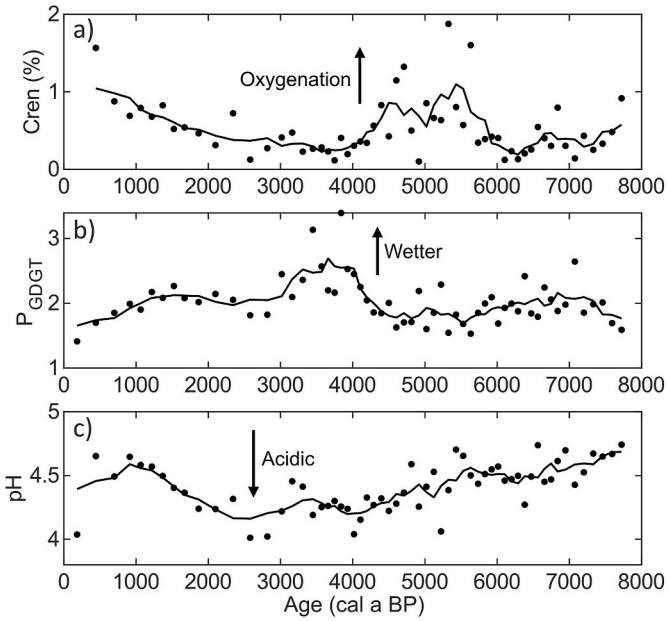

Fig. 3. GDGT indexes from the Padang peat sequence, including crenarchaeol (a), PGDGT (b), and reconstructed pH (c). The uppermost sample is not included in the crenarchaeol running mean because it is an outlier in terms of oxygenation/methanogenesis, likely due to a near-surface effect on the signal. Line plots are derived from a 5-point running mean.

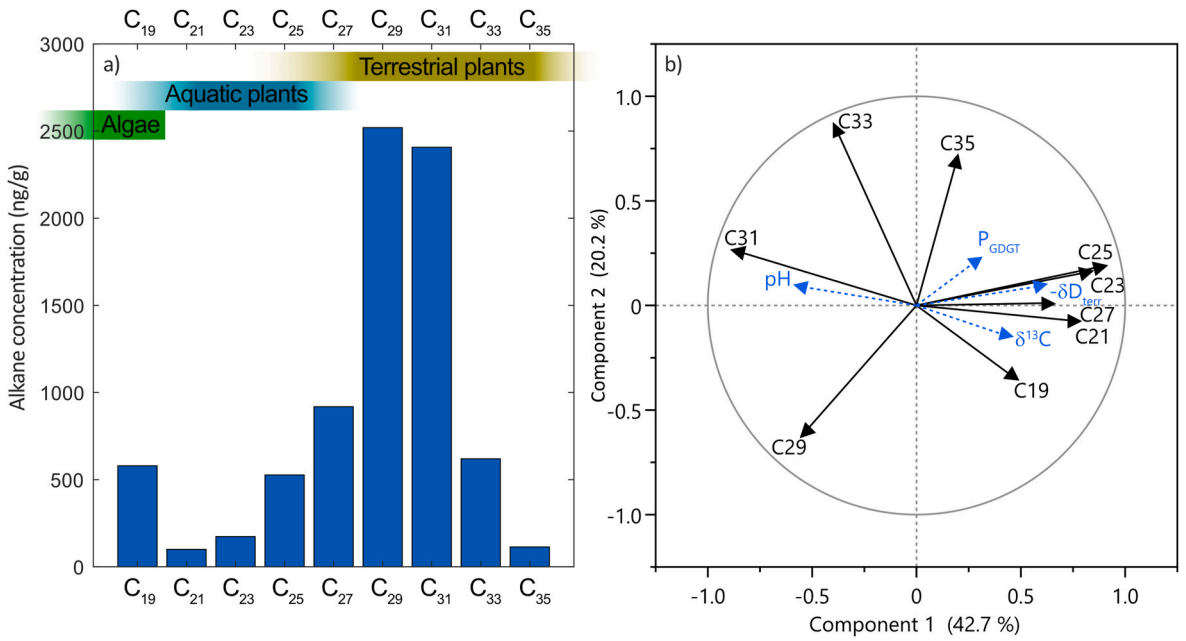

Fig. 4. Average *n*-alkane distribution (a) and PCA results from all samples (b). Tables of the loading matrix and supplementary variable coordinates are shown in Supplementary Table 1. The upper labels in (a) indicate the alkane producers, as further discussed in Section 4.1. Black labels in (b) are PCA loadings for each alkane, and blue labels are overlaid *a posteriori*.

alkanes. Down-core PC1 factor scores, $PC1_{alkanes}$, based on the PCA in Fig. 4, show the highest values around 3.5 cal ka BP, similar to $f(C_{21}$-$C_{27})$. $PC2_{alkanes}$ shows a gradual increase in the oldest and youngest parts of the record between 7.8 and 5.8 cal ka BP, and 3-0 cal ka BP, with two maximums around 6 and 3.3 cal ka BP, and lowest values around 4.5 cal ka BP (Supplementary Fig. 3).

3.4. Alkane hydrogen isotopes δD

The hydrogen isotopic composition of C_{19} to C_{33} alkanes was measured as a proxy for hydrological changes, of which we focus on δD_{terr} and δD_{C19} (Fig. 6). δD_{terr} has a decreasing trend after 7 cal ka BP from −171 ‰ to the lowest values of −212 ‰ between 4.3 and 3.3 cal ka BP. The Late Holocene is subsequently characterized by a rapid increase in δD_{terr} until ~2 cal ka BP to −169 ‰, followed by a slight decrease towards the present. In contrast, the δD_{C19} signal displays a distinct trend during the early parts of the record into the Mid-Holocene, with minimum values of −224 ‰ at ~5.5 cal ka BP and generally much lower δD_{C19} values than δD_{terr} in the early part of the record. δD_{C19} also displays rapid enrichment in deuterium at the start of the Late Holocene ~3 cal ka BP, similar to δD_{terr}. Broadly, all longer-chain alkanes (C_{25}-C_{33}) display similar δD trends over the whole record, i.e., the same general trends as δD_{terr} derived from C_{29} and C_{31}. For δD_{C21} and δD_{C23}, greater enrichment is also displayed at 6–5.5 cal ka BP, but we note that C_{21} and C_{23} generally have the lowest concentrations and were below the limit of quantification in many samples (see Supplementary Fig. 4 for the δD of all individual alkanes). The δD_{C21} and δD_{C23} records, therefore, consist of fewer data points than δD_{C19} and δD_{terr}.

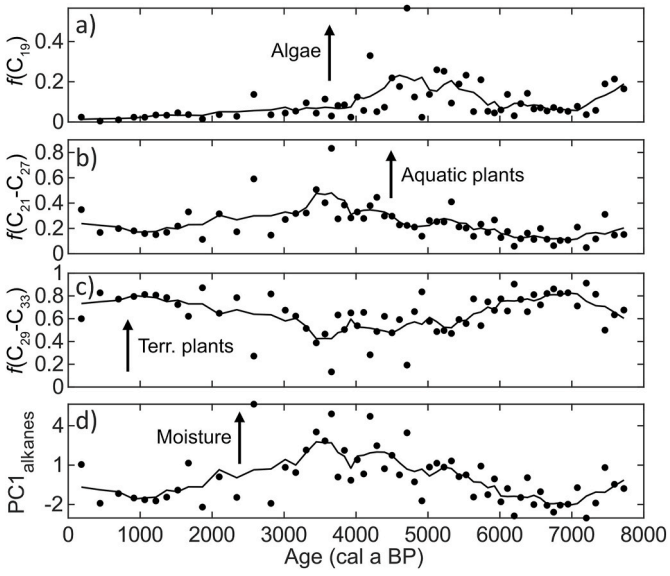

Fig. 5. Alkane indexes based on down-core relative abundances for (a) algal, (b) aquatic, and (c) terrestrial plant derived *n*-alkanes and (d) leading PC1 $_{alkanes}$ representing moisture. The circles show each data point, and the black lines are calculated as a 5-point running mean.

3.5. Biomass burning biomarkers

The concentration of levoglucosan ranged between 80 and 1100 ng g^{-1} dry sediment, except for one sample at 311–314 cm depth (4.74 ± 0.23 cal ka BP), which had a much higher concentration of levoglucosan at 14,500 ng g^{-1} (Fig. 7). The lowest concentration occurred at 191–194

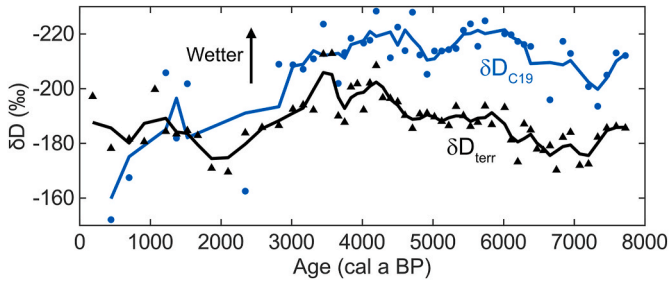

Fig. 6. δD_{C19} and δD_{terr} in the Padang peatland. Line plots are calculated as 3-point running mean, and each data point is shown as black triangles (δD_{terr}) and blue circles (δD_{C19}).

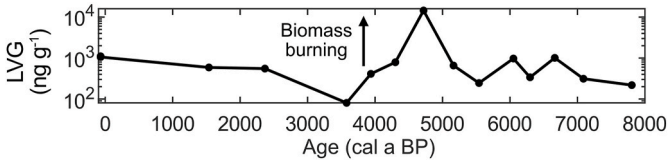

Fig. 7. Levoglucosan concentrations in the Padang peat core. Note that the scale is logarithmic.

cm depth (3.60 ± 0.22 cal ka BP). Mannosan and galactosan concentrations were lower than levoglucosan, but indicated the same trends over the whole record. The relative contributions of levoglucosan, mannosan and galactosan were around 65, 30 and 5%, respectively (Supplementary Fig. 5).

4. Discussion

In the discussion we first identify the sources of organic matter, linking biomass types to isotopic signals and vegetation dynamics in Sumatra. Next, we synthesize our hydrological results, focusing on annually integrated time scales. We then disentangle seasonal and annual hydrological signals and discuss what large-scale paleoclimatological mechanisms may have driven this variability. Lastly, we examine the implications of our findings for isotopic reconstructions in speleothem and leaf wax paleohydrological studies.

4.1. Vegetation and alkane sources

Our alkane compositional and GDGT data are governed by local vegetation and microbial communities, and therefore reflect local conditions on the Padang peatland (Figs. 4 and 5). Our findings are consistent with the vegetation described by Morley (1982), i.e., an herbaceous swamp surrounded by shrubs and forests. The most abundant *n*-alkanes were C_{29} and C_{31}, which are commonly produced in high quantities by terrestrial higher plants (Sachse et al., 2012). Considerable amounts of C_{25} and C_{27}, and to a smaller extent C_{21} and C_{23}, indicate the presence of aquatic macrophytes, i.e., aquatic plants that can be either submerged, floating, or emerged (growing below or above the water table) (Aichner et al., 2010; Ficken et al., 2000). A macrophyte source of all the mid-chain homologs is supported by that all C_{21} to C_{27} alkanes group together in the PCA on both PC1 and PC2. The high $f(C_{21}\text{-}C_{27})$ indicates that aquatic plants comprise a large fraction of the peat vegetation, consistent with over 60% cover of the macrophytic sedge *Machaerina rubiginosa* on the site (Morley, 1982).

There is also a significant amount of C_{19} alkane produced in the peat, and the C_{19} concentration reaches 600 ng g^{-1} on average, rivaling C_{25}, C_{33} and almost C_{27} in abundance. C_{19} has previously been found in aquatic settings (Cranwell et al., 1987; Zhang et al., 2019) but has also been reported in a tropical peat in Thailand (Yamoah et al., 2016) and in a subtropical peat in Eastern China (Pang et al., 2022). C_{19} alkanes have been found to be produced by green algae or anaerobic bacteria (Han et al., 1967), but is typically found in lower abundance compared to the C_{17} alkane. However, C_{17} was absent in the Padang core. Finally, C_{19} is reportedly also produced by some marine macrophytes (Dahl et al., 2024), but we are not aware of any reports of plants dominated by C_{19} alkanes present in tropical wetland ecosystems. The low abundance of C_{21} and C_{23} (produced by macrophytes), much larger abundance of C_{19}, and different behavior in the PCA (Fig. 4b), suggest that C_{19} derives from completely different source organisms than C_{21} and C_{23}. We therefore conclude that C_{19} in the Padang peat core is most likely produced predominantly by algae, in agreement with the interpretation by Yamoah et al. (2016). Importantly, we assert that the producers of C_{19} were aquatic organisms growing on the peatland during very wet, likely waterlogged, conditions. That C_{19} and C_{21}-C_{27} were produced by aquatic organisms (algae and macrophytes, respectively) is also supported by the correlation between their abundances and the precipitation proxies δD_{terr} and P_{GDGT} (Fig. 4b), i.e., more aquatic alkanes are produced during wet periods (further discussed in Sections 4.2 and 4.3). There is a large spread in the PCA among the longest chain *n*-alkanes, particularly between C_{29} and C_{31} versus C_{33} and C_{35}. This spread suggests different sources, which likely represent woody plants (C_{29} and C_{31} primarily) versus a grass source (C_{33} and C_{35} primarily) (Diefendorf and Freimuth, 2017). Following this observation, $PC2_{alkanes}$ (Supplementary Fig. 3) likely represent the variability between grassy and woody vegetation at the core site. A correlation matrix between alkane concentrations and alkane δD values is presented in Supplementary Table 3.

Furthermore, $f(C_{21}\text{-}C_{27})$ correlates with GDGT derived pH, i.e., more acidic conditions prevail when macrophytes and algae were more abundant. This pH – vegetation relationship is consistent with the expectation that organic acids builds up under waterlogged conditions, and conversely, pH increases during drier periods when the peat may be more oxygenated. Likewise, $\delta^{13}C$ also correlates with $f(C_{21}\text{-}C_{27})$ (Fig. 4b), which agrees with the findings that macrophytes and algae have higher $\delta^{13}C$ values than terrestrial plants. We note, however, that the $\delta^{13}C$ variability is small (~1 ‰), suggesting generally stable wetland vegetation.

4.2. Annual hydroclimate

Precipitation water isotopes have previously been found to correlate predominantly with regional climate, reflecting convection strength, moisture sources and circulation patterns (Kurita et al., 2009; Konecky et al., 2016; Belgaman et al., 2017). The isotopic signature of the source water available for primary production is subsequently affected by evapotranspiration which causes enrichment of the heavy isotopes, especially during dry periods (Sachse et al., 2012). Since C_{29} and C_{31} are mostly produced by terrestrial perennial (multi-year growth) vegetation (Malhi et al., 2014b), we interpret the δD_{terr} to be indicative of an annually integrated isotopic signal (Sachse et al., 2012; Feakins et al., 2016), in agreement with findings in tropical Africa by Griepentrog et al. (2019). While a seasonal component of our δD_{terr} is possible (Feakins et al., 2016; Konecky et al., 2016; Sachse et al., 2012, 2015), its contribution is likely small relative to the 43 ‰ range in δD_{terr} shifts over the Holocene, since plant growth in Sumatra occurs over the whole year. Dry season evaporation may cause increased δD_{terr} in a more seasonally dry climate, causing a strengthened drying signal (Sachse et al., 2012), but whether this effect had a significant impact on our Sumatran reconstruction is challenging to quantify without multi-year monitoring of how δD_{wax} responds to seasonal changes. However, a significant bias towards the wet season can probably be ruled out – in which case δD_{terr} would be more similar to δD_{C19}. Likewise, a significant dry season bias in our δD_{terr} data seems unlikely, as that would be at odds with the climate model simulation data and our understanding of a positive relationship between precipitation and insolation (see section 4.4). Additionally, our δD_{terr} and δD_{C19} interpretations are supported by our independent multiproxy data both in terms of annual and seasonal wetness (see below), indicating that our interpretation is robust.

δD_{terr} decreases after 7 cal ka BP (Fig. 6), indicating increasingly strong convection and wetter conditions reaching peak precipitation between 4.5 and 3 cal ka BP. After this wettest period, rapid drying is indicated by rising δD values. The δD_{C19} record, based on algal alkanes, also indicates wetter conditions after 7 cal ka BP and the same distinct drying after 3 cal ka BP. However, the pattern for δD_{C19} is different from δD_{terr}, with a faster decrease, indicating an earlier precipitation maximum, and overall lower values than δD_{terr} until ~2.5 cal ka BP. The mid-chain (C_{25}, C_{27}) *n*-alkanes exhibit values that are in between those of δD_{terr} and δC_{19} (Supplementary Fig. 4 for δD signals from all individual alkanes). During the Late Holocene, δD_{C19} and δD_{terr} are in general agreement in terms of absolute values. The explanation for the different evolution of the δD_{terr} and δC_{19} records must lie in a changing distribution of precipitation throughout the year, combined with a

changing degree of isotope enrichment caused by evapotranspiration, i.e., a change in the seasonality of rainfall amount and convective activity, and length and/or intensity of dry season (further discussed in Section 4.3).

More insight into hydroclimate dynamics can be gained by evaluating the non-isotopic aspects of our multi-proxy record. The first principal component ($PC1_{alkanes}$) in the PCA of the alkane distributional data mainly reflects the abundance of mid-chain *n*-alkanes (C_{21}-C_{27}) and C_{19} relative to the longer *n*-alkanes (C_{29}, C_{31} and C_{33}) (Fig. 4). We interpret this to be a local moisture signal reflecting the abundance of organisms requiring wet conditions (aquatic macrophytes and algae) versus terrestrial plants which are not as sensitive to drying. $PC1_{alkanes}$ is therefore a proxy for the wetland water balance at the site, with positive values indicating wet, and negative values indicating dry conditions (Figs. 4 and 8). $PC1_{alkanes}$ indicates the wettest conditions occurred between 4.5 and 3 cal ka BP, in agreement with δD_{terr}. Based on the recently suggested P_{GDGT} index (De Jonge et al., 2024), the GDGTs also indicate wetter conditions between 4 and 3 cal ka BP, and drier conditions during the early stages of the Mid-Holocene and the Late Holocene. Our multi-proxy results therefore confirm that the P_{GDGT} index works as proxy for wetness, and is, in addition to soils, also applicable to peat records. The P_{GDGT} index suggests the wettest overall conditions at ~3.8 cal ka BP, similar to the $PC1_{alkanes}$ and δD_{terr}.

Our multi-proxy approach thereby yields three independent estimates of annually integrated humidity, namely, P_{GDGT}, $PC1_{alkanes}$, and δD_{terr}. In synthesis, peak humidity occurred between 4.5 and 3 cal ka BP, and significantly drier conditions prevailed between 8 and 6 cal ka BP and during the Late Holocene (from ~2.8 cal ka BP) (Fig. 8). The consistency between these three proxies gives high confidence that they reflect the trends of precipitation on Sumatra over the Holocene. Our record is in general agreement with major trends reconstructed at other equatorial sites in the IPWP (Dang et al., 2020; Wurtzel et al., 2018; Partin et al., 2007; Yuan et al., 2023; Konecky et al., 2016). However, an offset in the timing of peak precipitation is observed compared to speleothem records (Fig. 9 e, f, g), which is further discussed in Section 4.5.

In terms of mechanisms for maximum annual precipitation in Sumatra between 4.5 and 3 cal ka BP, a reorganization of the Asian monsoon system is a likely candidate. A collapse of the Asian Summer Monsoon (ASM) over mainland southern Asia has been suggested around 4.3 cal ka BP (Griffiths et al., 2020), which is synchronous with the onset of peak precipitation in Sumatra. Multiproxy stacks reflecting the EASM and EAWM (Fig. 9p and q) in China (Kaboth-Bahr et al., 2021) show an inverse pattern to Sumatra, with much weaker monsoonal activity synchronous with peaking Sumatran precipitation. The monsoon stacks closely mirror the precipitation and humidity proxies we reconstruct in Sumatra (Fig. 9a–p and q). Griffiths et al. (2020) suggest that the collapse of the ASM (Fig. 9o) was tied to the end of the African Humid Period and the collapse of Green Sahara (Fig. 9k), based on climate model simulations and the speleothem record in Laos. This collapse led to cooling of the Indian Ocean and consequently weakened monsoonal precipitation in the northern hemisphere, causing a southward shift of boreal monsoon precipitation and a contracted ITCZ (Fig. 9r) (Griffiths et al., 2020; Yuan et al., 2023). A southward shift of the precipitation due to a collapse of the ASM and contraction of the ITCZ, causing a concentration of precipitation towards the equator, therefore provides potential mechanisms for the overall wetter conditions recorded in our core between 4.5 and 3 cal ka BP. This is in agreement with the increased ITCZ driven precipitation caused by

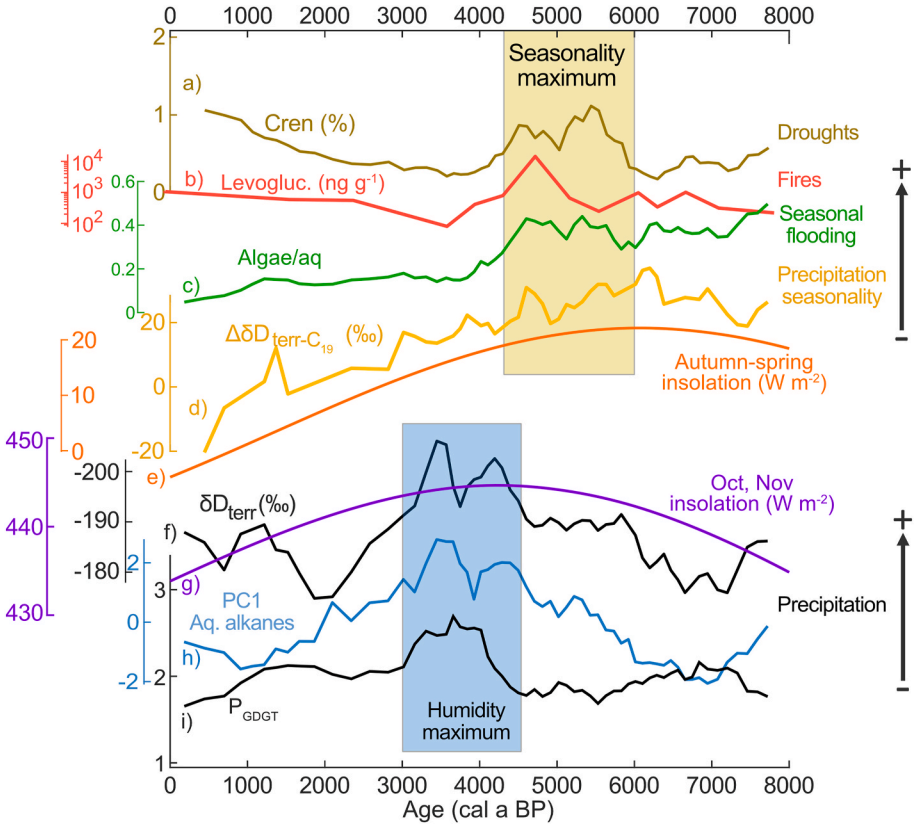

Fig. 8. Synthesis of the hydroclimatological data from the Padang wetland and orbital insolation at 2 °S. Indicators for seasonality in a–e: (a) crenarchaeol fractional abundance, (b) levoglucosan concentration, (c) algae/aquatic *n*-alkane ratio, (d) $\Delta\delta D_{terr\text{-}C19}$, (e) insolation difference between September to December and January to April at 2 °S (Laskar et al., 2004). Indicators for more annually integrated precipitation or humidity in f–i: (f) δD_{terr}, (g) October to November insolation at 2 °S, (h) $PC1_{alkanes}$ reflecting aquatic *n*-alkanes, and (i) P_{GDGT}, precipitation proxy based on GDGTs. A three-point smoothing is applied to the isotopic records ($\Delta\delta D_{terr\text{-}C19}$, δD_{terr}), and a five-point smoothing is applied to cren, algae/aq, $PC1_{alkanes}$ and P_{GDGT}.

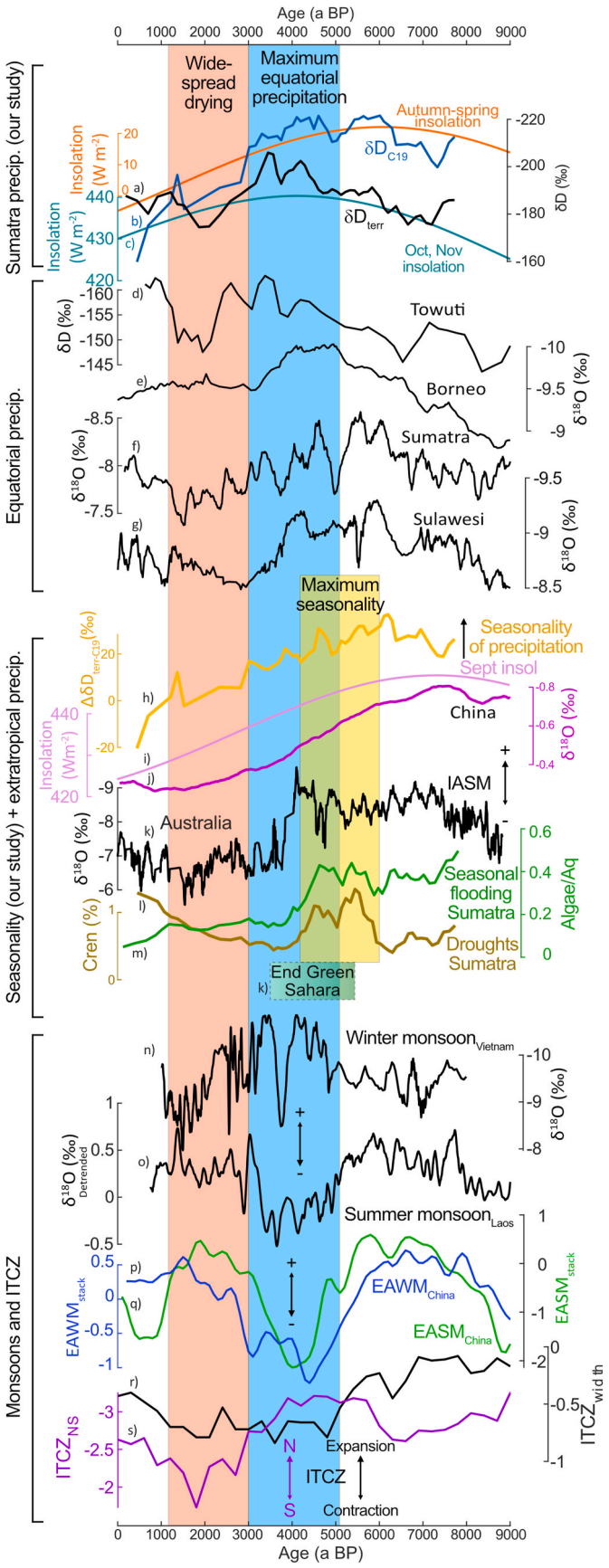

(caption on next column)

Fig. 9. Regional proxy comparison, including our reconstructions, other δD_{wax} reconstructions, speleothem $\delta^{18}O$ and monsoon stacks. Records (a) and (b) are the *n*-alkane δD_{terr} and δD_{algae} from Sumatra (this study). c) shows the insolation at 2 °S during October and November, and SOND-JFMA. d) is a δD_{wax} from lake Towuti on Sulawesi (Konecky et al., 2016). e) Borneo speleothem (Partin et al., 2007). f) Sumatran speleothem (Wurtzel et al., 2018). g) Sulawesi speleothem (Yuan et al., 2023). h) $\Delta\delta D_{terr\text{-}C19}$ seasonality index reconstructed in Sumatra (this study). i) equatorial insolation in September (Laskar et al., 2004). j) Chinese speleothem stack (Yang et al., 2019) k) Australian speleothem (Denniston et al., 2013). l and m) seasonal droughts and floods in Sumatra (this study). n) Vietnam speleothem, indicative of Asian winter monsoon precipitation (Wolf et al., 2023). o) Laos speleothem, processed with a linear detrend, indicative of Asian summer monsoon precipitation (Griffiths et al., 2020). p) and q) East Asian winter and summer monsoon stacks (Kaboth-Bahr et al., 2021). r) and s) ITCZ variability position and width (Yuan et al., 2023). A three-point smoothing is applied to the *n*-alkane isotopic records (δD Towuti (Konecky et al., 2016) and δD_{C19}, $\Delta\delta D_{terr\text{-}C19}$, δD_{terr} from this study) and the EAWM/EASM stacks (Kaboth-Bahr et al., 2021) and a five-point smoothing is applied to cren, algae/aq, $PC1_{alkanes}$ and P_{GDGT}, and a ten-point smoothing was used on all speleothem records. Different smoothing windows were used due to the differences in temporal resolution between records.

heating of the eastern parts of the IPWP reconstructed and simulated by Dang et al. (2020). They attribute the warming and wetting in the IPWP to a strengthening of the Pacific Walker Circulation in the Mid-Holocene driven by autumn insolation. A stronger Walker Circulation increased the Pacific Ocean temperature gradient, warmed the West Pacific Ocean temperatures and caused increased convection over the IPWP.

Rapid drying in the IPWP region has been recorded around 2.5 cal ka BP in several records: Sumatra δD (this study), Sumatra speleothem $\delta^{18}O$ (Wurtzel et al., 2018), Borneo (Partin et al., 2007) and on Sulawesi (Konecky et al., 2016; Parish et al., 2024) (Fig. 9 a, b, d-g) and according to a climate model simulation and seawater $\delta^{18}O$ (Dang et al., 2020). The drying occurred when the IASM weakened(Steinke et al., 2014) and the boreal monsoons re-strengthened (Griffiths et al., 2020; Kaboth-Bahr et al., 2021), i.e., humidity was exported northward from the equator. At the same time, the ITCZ rapidly shifted southwards and expanded to an extent more similar to the present climate due to cooling in the northern hemisphere (Griffiths et al., 2020; Yuan et al., 2023). The expansion and southward shift of the ITCZ and equatorial drying also shifted the precipitation further south to Flores (8 °S), which became wetter at the same time as the rest of the region dried (Griffiths et al., 2013). The Pacific Walker Circulation also became weaker during the Late Holocene, causing a weaker ascending branch of the Walker Circulation and lower convection over the IPWP (Dang et al., 2020). Notably, this rapid drying occurs simultaneously with the strengthening of ENSO variability over the Pacific region (Carré et al., 2021; Emile-Geay et al., 2016). This suggests important interdependencies between the IPWP and Asian-Australian monsoon systems, and the Walker Circulation, but these relationships lie outside the scope of this study.

4.3. Seasonality

We interpret δD_{terr} as an annually integrated signal, while δD_{C19} predominantly reflects the water isotopic signal from the wettest season (boreal autumn to winter; Fig. 1) with a flooded peat surface with favorable conditions for algal blooms. During the rainy season, heavy rainfall may also bring nutrients to the wetland from surrounding soils as a result of erosional transport, further supporting algal growth. To quantify the differences between the annual and wet season signals, we calculate $\Delta\delta D_{terr\text{-}C19}$ (Eq. (8)):

$$\Delta\delta D_{terr-C19} = \delta D_{terr} - \delta D_{C19} \quad (8)$$

The $\Delta\delta D_{terr\text{-}C19}$ index reflects qualitative changes in the difference between precipitation from the entire year and the rainy season (Fig. 8d and 9h). Positive values of $\Delta\delta D_{terr\text{-}C19}$ indicate a bias towards low δD_{precip} values in the wet season. Moreover, the annual signal from δD_{terr}

should experience a stronger influence from deuterium isotope enrichment during the dry season, leading to a higher $\Delta\delta D_{terr\text{-}C19}$ in a seasonal climate. The $\Delta\delta D_{terr\text{-}C19}$ is a proxy for seasonality, where high values indicate a large difference in precipitation between the wet and dry seasons, and low values indicate a more equable hydroclimate throughout the year. The $\Delta\delta D_{terr\text{-}C19}$ curve (Fig. 8d) indicates high seasonal differences during the Mid-Holocene, which gradually decreases over the Holocene, with the lowest values towards the present day. This isotopic index indicates that seasonal differences peaked around 6 cal ka BP.

We further explore seasonality signals in our multi-proxy dataset in terms of alkane composition. As discussed earlier, C_{19} is most likely produced by algae, which mainly grows during the wet season, potentially during flooding and input of nutrients. Interestingly, $f(C_{19})$ peaks earlier than the three annual wetness proxies discussed in Section 4.1, even though they all, including $f(C_{19})$, are driven by varying aspects of moisture. Aquatic macrophytes, which produce C_{21} to C_{27} in this setting, are perennial and grow throughout the year and, therefore, require extended periods of wet conditions to thrive, rather than just during shorter periods of standing water, like algae. Although $f(C_{19})$ and $f(C_{21}\text{-}C_{27})$ generally correlate in our core (Figs. 4 and 5), there is a ~1.5 kyr offset when they peak, with higher $f(C_{19})$ abundances when $f(C_{21}\text{-}C_{27})$ are still relatively low in concentration (Fig. 5). We analyze the differences in $f(C_{19})$ and $f(C_{21}\text{-}C_{27})$ by calculating the algae/aq ratio (Eq. (9)).

$$Algae\,/\,aq = \frac{[C_{19}]}{\sum [C_{19}\text{ to }C_{27}]} \tag{9}$$

This index quantifies the ratio between algal and macrophyte alkane concentrations, and thereby reflects the seasonal wetness (flooding alternated by drier conditions) versus long term humid conditions. The algae/aq ratio (Figs. 8c and 9m) is, therefore, a seasonality proxy independent from the $\Delta\delta D_{terr\text{-}C19}$ index discussed above. Algae/aq shows a clear trend towards more seasonal flooding in the Mid-Holocene compared to the Late Holocene. In particular, algal production peaks prominently between ~5.8–4.2 cal ka BP, a period otherwise characterized by relatively low macrophyte production (Fig. 5), and is high in the entire period 8–4.2 cal ka BP. This suggests at least seasonally relatively dry conditions interrupted by seasonal flooding during which algae were produced.

Furthermore, crenarchaeol, interpreted as a proxy for dry conditions (Hällberg et al., 2023), peaks between 5.8 and 4.2 cal ka BP, i.e., at exactly the same time as the algae/aq ratio suggests seasonal flooding. We therefore have evidence for synchronous seasonal flooding and seasonal droughts co-occurring in the Mid-Holocene – i.e., a highly seasonal climate with enhanced rainfall during the wet season and increasing dry conditions in the dry season – in line with the inferred increased seasonality of the $\Delta\delta D_{terr\text{-}C19}$ record.

The presence of levoglucosan, and the other monosaccharide anhydrides, throughout the record indicates that biomass burning occurred in the region throughout the investigated period. These compounds can travel long distances as aerosols and are not very stable in oxygenated soils (Norström et al., 2021), and we therefore argue that it has a dominantly aeolian origin. The around 20 times higher levoglucosan concentration found at 4.7 cal ka BP compared to the rest of the period indicates a local biomass burning event. This event coincides with the slightly higher mineral content of the peat, which leads us to speculate the area did burn locally, and that this disturbance led to some erosion from the surrounding area onto the peatland, likely aided by the stronger seasonality of this period. The lowest levoglucosan concentration was observed around 3.6 cal ka BP, when the hydroclimate had just shifted to being less seasonal although still very humid (Fig. 8b), which is unfavorable for biomass burning. The levoglucosan results thus corroborate the other proxies for seasonality.

The synthesis of our results (Fig. 8) indicates a relatively dry Mid Holocene (8–4.2 cal ka BP) with increasing seasonality that peaked between ~6–4.2 cal ka BP caused both by increasing precipitation but continued seasonal dryness. The maximum regional precipitation and wettest peatland conditions throughout the year occurred synchronously between 4.5 and 3 cal ka BP. The regional climate then transitioned relatively fast towards significantly drier conditions in the Late Holocene, but with more evenly distributed precipitation throughout the year.

4.4. Mechanisms for precipitation seasonality

It has previously been found that the precessional cycle exerts a dominant forcing on tropical climate (Mohtadi et al., 2016) and that precipitation reconstructions from the IPWP closely follow autumn insolation, i.e., the period with the highest precipitation (Djamil et al., 2023). This relationship between maximum precipitation and wet season insolation has been observed in many places, including the IPWP, China and Australia (Denniston et al., 2013; Partin et al., 2007; Wolf et al., 2023; Yang et al., 2019; Yuan et al., 2023), and is consistent with modeling studies (Dang et al., 2020; He, 2011). Dang et al. (2020) found that insolation was a major driver of rainfall variability in the IPWP over the Holocene, based on a CESM simulation forced solely by changes in insolation. Indeed, the maximum precipitation at our site, inferred from δD_{terr}, $P_{GDGT,}$ and $PC1_{alkanes}$, occurs when the October–November insolation is at its peak, around 4 cal ka BP (Fig. 8), corresponding to the onset of the rainy season in the current climate state (Fig. 1).

However, insolation during the spring equinox around March is also important for the water balance in Sumatra, when a second precipitation maximum occurs during the northward passing of the ITCZ (Fig. 1). At present day, the whole period from September through April receives more rainfall relative to the summer, thus causing a relatively long wet period, and short dry period during the boreal summer (Fig. 1). However, in the Mid-Holocene, this was likely significantly altered, with a more intense wet season, and longer dry season, caused by altered seasonal distribution of insolation. Insolation at 2 °S during the boreal winter-spring period (JFM) was significantly lower during 8-5 cal ka BP compared to the present (-21.8 W m^{-2} or -5.0 %) (Fig. 10) (Laskar et al., 2004). Based on the positive relationship between insolation and precipitation (Hällberg et al., 2022; Mohtadi et al., 2016), this likely led to reduced convection and drier conditions in the months leading up to the dry period of June–August, resulting in a longer and stronger drying of the peatland, as evidenced by the crenarchaeol drought proxy (Figs. 8 and 9). On the other hand, insolation around the autumn equinox (ASO) was stronger during this time (+20.2 W m^{-2} or +4.8 %), leading to stronger convection and wetter conditions in autumn causing stronger flooding of the area, allowing algal growth as evidenced by the $f(C_{19})$ record. The difference between the mean monthly insolation during autumn and spring (ASO- JFM or SOND-JFMA) (Fig. 8e and 9c) follows the seasonality reconstructed by $\Delta\delta D_{terr\text{-}C19}$. After 4 cal ka BP, the seasonal difference was reduced both by the decrease of autumn insolation and the increase during spring, leading to a more equal distribution of rainfall over the entire September–April period we see today (Figs. 1 and 10).

To test the hypothesis that insolation was a key driver of hydrological changes in Sumatra and the Maritime Continent over the Holocene, we analyzed the transient MPI-ESM1.2 climate model simulation over the past 8000 years (Bader et al., 2020; Dallmeyer et al., 2021). The model reproduces the major trends in annual precipitation reconstructed by proxies (this study, Wurtzel et al., 2018; Partin et al., 2007; Yuan et al., 2023): a relatively dry start of the Mid-Holocene, wettest conditions during the later parts of the Mid-Holocene as wet season insolation peaked, and drying in the Late Holocene (Fig. 11a and b). However, the change in annual precipitation is only approximately 100 mm over the study period, amounting to a ~3 % change. That the amplitude of simulated rainfall change is relatively minor over the study period is potentially related to the fact that decreasing autumn precipitation was compensated by increasing precipitation during spring in the Late Holocene. The annual precipitation trends are also spatially heterogeneous

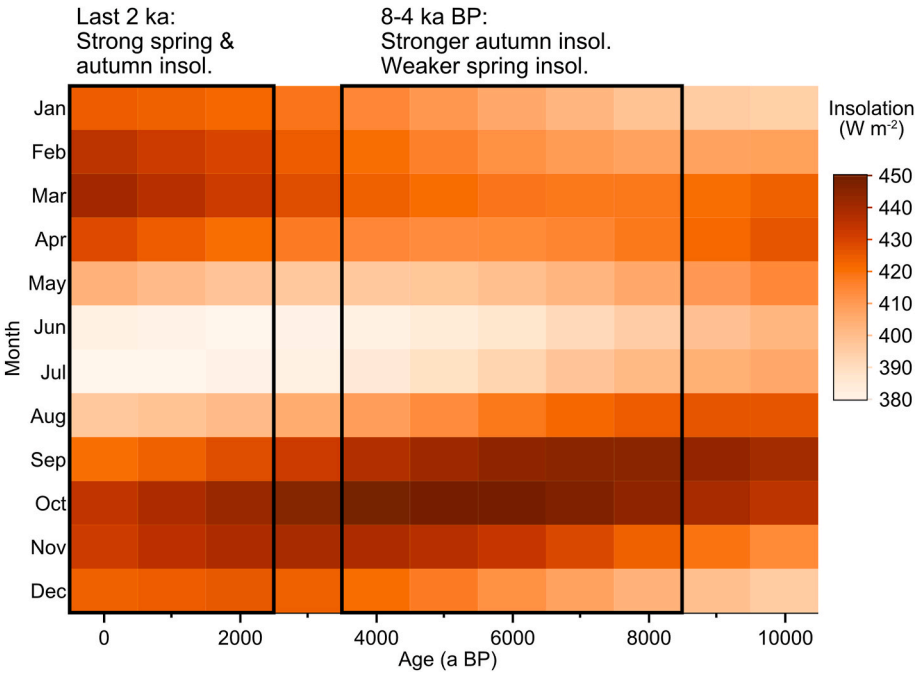

Fig. 10. Monthly insolation over the past 10 kyr at 2° S, showing the different distribution of seasonal insolation over time. The seasonally uneven energy distribution in the mid-Holocene increases the likelihood for longer dry seasons compared to today even if total annual precipitation is higher. Data derived from Laskar et al. (2004).

over the region, and the timing of simulated peaking precipitation is earlier if the model data is averaged over a small field in Sumatra (around 4.5 cal ka BP) compared to a larger field integrated over the Maritime Continent (4.4–2.2 cal ka BP) (Fig. 11a and b). This is because the western parts of the Maritime Continent received more rainfall in the Mid-Holocene, and the eastern Maritime Continent received higher precipitation in the later parts of the Holocene due to a simulated eastward shift of deep convection over the study period.

The meridional location of the annual precipitation maxima is shifted southwards over the Holocene according to the model results, consistent with a southward shift in the ITCZ when boreal temperatures decreased over the Holocene (Kaufman et al., 2020), as also found for the Flores speleothem reconstruction (Griffiths et al., 2013) and an ITCZ reconstruction (Fig. 9s: Yuan et al., 2023). Both the eastward shifted convection center over the Maritime Continent and the southward shifted ITCZ thereby contributed to the simulated (this study) and reconstructed (this study, Wurtzel et al., 2018) drying during the Late Holocene in Sumatra. These two mechanisms resulted in an annually

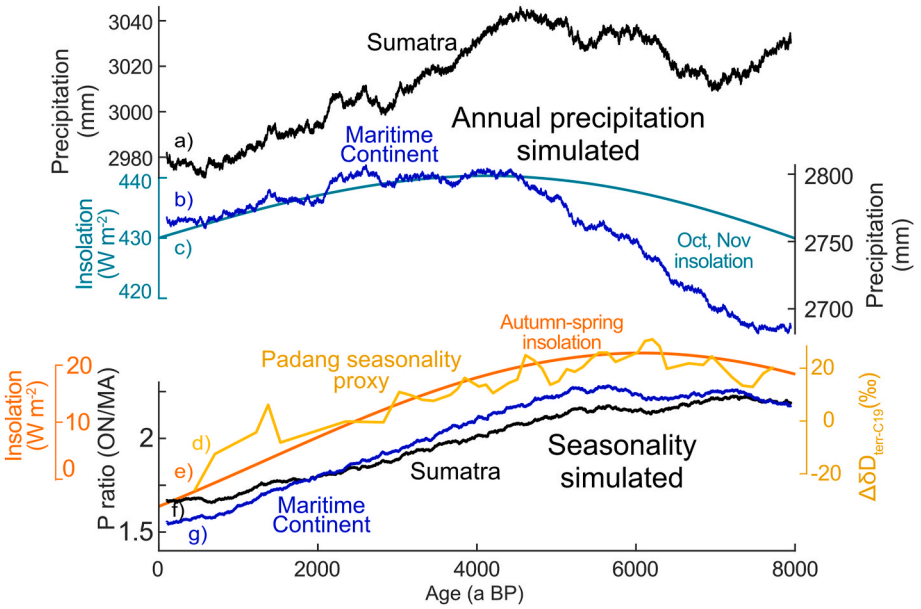

Fig. 11. Simulated annual amount and seasonality of precipitation over the past 8000 years, compared to reconstructed seasonality and insolation. Simulated annual precipitation for (a) Sumatra and (b) a larger area over the Maritime continent. (c) October and November insolation at 2 °S. (d) $\Delta\delta D_{terr\text{-}C19}$ precipitation seasonality proxy. (e) Insolation difference between autumn (SOND) and spring (JFMA). Simulated precipitation seasonality is expressed via the autumn/spring (ON/MA) precipitation ratio for (f) Sumatra and (g) the Maritime Continent. The model output of MPI-ESM 1.2 (Bader et al., 2020; Dallmeyer et al., 2021) for Sumatra was derived from 96 to 107 °E, 7 °S-3 °N, and for the Maritime Continent from 100 to 125 °E, 5 °S-5 °N (see Fig. 12). Insolation for October and November.

integrated drying caused by IASM weakening at equatorial Sumatra during the Late Holocene. This is consistent with the reconstructed IASM weakening in Australia (Fig. 9 k: Denniston et al., 2013).

In contrast to total precipitation, there were significant changes in the seasonal distribution of precipitation over the study period. These changes were uniform over most of the Maritime Continent. The Mid-Holocene was characterized by much stronger precipitation during autumn (September, October and November) and less precipitation during spring (March, April, May) than the Late Holocene (Fig. 11c and d, Supplementary Fig. 6). Both the wet and dry periods, i.e., the IASM and IAWM were thereby lengthened according to the model results, consistent with an orbital forcing driver discussed above, and our multiproxy reconstructions of seasonality. The precipitation for all months is shown in Supplementary Fig. 6. The orbital forcing exerted by the precessional cycle thus appears to be a major driver of the seasonal hydroclimate evolution at our site in Sumatra. This caused a strong imprint on the annual cycle of the peatland's water balance, with greater seasonal differences in the Mid-Holocene compared to today and the past two millennia.

The increase of seasonal floods we reconstruct in Sumatra between 6 and 4.2 cal ka BP are linked to stronger autumn/winter precipitation due to an intensification of ITCZ precipitation (Yuan et al., 2023) and lengthening of wet period associated with the IASM and northeastern monsoon (NEM) circulation. Wolf et al. (2023) reconstructed the NEM from Vietnam and found increased precipitation sourced from the South China Sea and Pacific during the boreal winter months, similar to the increase in precipitation we reconstruct in Sumatra (Fig. 9 n). The extension of the NEM into the southern hemisphere in Sumatra is the IASM which brings most of the boreal autumn/winter precipitation, i.e., the wettest season in Sumatra (Wurtzel et al., 2018). The MPI-ESM1.2 model results indicate that the strengthened NEM, recorded in the Vietnam speleothem, was not associated with a stronger northeasterly winds and moisture export to Sumatra. In fact, the northeasterly winds weakened over the South China Sea and the Gulf of Thailand (Fig. 12a). Instead, the increased precipitation was sourced mainly from the Indian Ocean (Fig. 12). The IASM circulation transports moist and warm tropical air from the IPWP to Australia and brings northeasterly winds and rain across Indonesia and Sumatra. Denniston et al. (2013) reported large peaks in IASM strength between ~4.8–4.1 ka based on Australian speleothems (Fig. 9 k). This is synchronous within age model error with the peaks in flooding recorded in Padang, suggesting a strong link between IASM strength over Australia and seasonal precipitation in Sumatra, on short and long timescales.

4.5. Implications for interpretation of isotopic records

Our Sumatran site is located only ~150 km from the Tangga Cave speleothem (Wurtzel et al., 2018), and we would therefore expect similar results in reconstructed precipitation. However, as observed with the various rainfall proxies at our site, the speleothem and biomarker proxies behave differently. The discrepancy is likely due to different sensitivity towards different aspects of hydroclimate, i.e., total rainfall, seasonal drought or seasonal wetness. The Sumatran $\delta^{18}O_{speleo}$ record by Wurtzel et al. (2018) follows our δD_{C19} (and $\Delta\delta D_{terr\text{-}C19}$) seasonality records closely, but not the δD_{terr} which we interpret to reflect an annually integrated signal. Following our argument that the δD_{C19} reflects primarily the wet season, we propose that the Sumatran speleothem may be more influenced by seasonality over the Holocene than previously established. Wurtzel et al. (2018) focus mainly on Late Pleistocene deglacial changes, and interpret their $\delta^{18}O$ record to reflect annually amount weighted average $\delta^{18}O_{rainwater}$ as well as from changes in moisture sources and upstream moisture trajectories. Higher $\delta^{18}O$ in their speleothem was thereby interpreted as drying (amount effect), as well as shorter moisture trajectories during the boreal summer monsoon for the deglacial period. Following this reasoning, our data suggests that during the Holocene, the intensified boreal winter precipitation (IASM) had the opposite effect, resulting in decreased $\delta^{18}O$ in the Mid-Holocene due to seasonal wetting, i.e., a mix of amount and (seasonal) source effects.

Although there have been numerous studies in the tropics monitoring modern cave dripwater $\delta^{18}O$ variability (Cobb et al., 2007; Ellis et al., 2020; Lases-Hernandez et al., 2019; Moerman et al., 2013, 2014; Ridley et al., 2015) and discussing seasonality and the controls of speleothem $\delta^{18}O$ over glacial-interglacial timescales (Krause et al., 2019; Partin et al., 2007; Theaker et al., 2024; Wurtzel et al., 2018), it has remained challenging to disentangle seasonal versus annual influences based on proxy data, in particular over the Holocene. The importance of seasonality for speleothems is established at some tropical sites (Baker et al., 2019), and for example Patterson et al. (2023) and Wolf et al. (2023) interpreted speleothems in Vietnam to be driven by boreal winter monsoonal water isotope composition, with a negligible input from the summer monsoon precipitation, but it is low or insignificant at lower-seasonality sites (Yuan et al., 2023; Theaker et al., 2024).

Cave dripwater $\delta^{18}O$ varies in concert with $\delta^{18}O_{rainwater}$, which reflects regional convection and precipitation (Moerman et al., 2013; Cobb et al., 2007; Wolf et al., 2020; Johnson et al., 2006; Belgaman et al., 2017). Cave dripwater, and thereby speleothem carbonate reflects precipitation isotopes during recent precipitation on timescales from days to months, or up to years in caves depending on recharge rates or reservoir size. Cave water recharge time can accordingly occur at

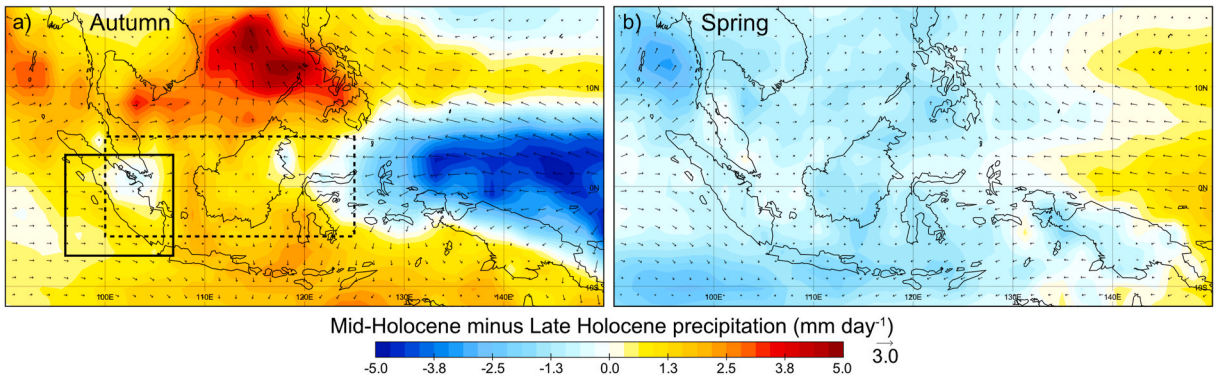

Fig. 12. Simulated changes in precipitation and surface mean winds between the Mid to Late Holocene for autumn and spring. Difference in precipitation (shaded colors) and surface winds (vectors) between 6 and 4 cal ka BP and 2-0 cal ka BP during (a) autumn (Oct, Nov) and (b) spring (April, May). Red (blue) colors indicate that 6-4 cal ka BP was wetter (drier) than 2-0 cal ka BP. Wind vectors pointing northward (westward) indicate strengthened northward (westward) winds, or weakened southward (eastward) winds at 6-4 cal ka BP relative to 2-0 cal ka BP, i.e., represent the changes in wind strengths. Model data from MPI-ESM (Bader et al., 2020; Dallmeyer et al., 2021), used in Fig. 11 was derived from Sumatra (small box, solid line) and the Maritime Continent (large box, dashed line) in (a).

seasonal time scales in the IPWP and South America (Belgaman et al., 2017; Cobb et al., 2007; Ellis et al., 2020; Jiménez-Iñiguez et al., 2022; Lases-Hernandez et al., 2019; Moerman et al., 2014). For example, a 3–18-month recharge time has been estimated for three different drips on Borneo (Moerman et al., 2014; Ellis et al., 2020), and speleothems can in some cases thereby capture event to seasonal time scale precipitation isotopes. Weather events associated with ENSO and Madden-Julien Oscillation downpours and droughts cause isotopic excursions in $\delta^{18}O$ of precipitation as well as in cave dripwater on Borneo (Moerman et al., 2013, 2014), and high resolution sampling of speleothem δ18O has thereby been used as a proxy for seasonal ENSO variability over the Holocene (Chen et al., 2016; Theaker et al., 2024). During dry periods, speleothem growth may even stop completely (Chawchai et al., 2021). Thereby, changes in dry season length or wet season intensity or moisture source changes over millennial time scales likely affect the integrated $\delta^{18}O$ signal recorded by speleothems (see e.g. Wurtzel et al., 2018).

Several studies suggest a seasonally dominated signal in speleothems, and an important influence of source changes (Liu et al., 2023; Qiu et al., 2023; Tian et al., 2023; Zhang et al., 2018). In line with orbital forcing of precipitation in the Asian monsoon system, including in the IPWP and China, our Sumatran $\Delta\delta D_{terr\text{-}C19}$ seasonality record closely matches Chinese speleothem records (Yang et al., 2019). In Sumatra, the precipitation seasonality is much smaller than in China, and the seasonality effect on speleothem growth is therefore likely smaller, but may explain the ~1500–2000 year offset between our Padang δD_{terr} and the Tangga Cave $\delta^{18}O_{speleo}$. A seasonal effect on speleothem growth is consistent with dripwater measurements on Borneo, which show a 2–3 ‰ $\delta^{18}O_{speleo}$ seasonal cycle (Moerman et al., 2014; Cobb et al., 2007), corresponding to ~16–24 ‰ in water δD (based on the meteoric water line; Kurita et al., 2009). Seasonal bias in the deposition of speleothem carbonate may occur depending on the variability in calcium saturation state and cave air and drip water pCO_2 over the year (Lachniet, 2009). A similar offset between δD_{wax} and $\delta^{18}O_{speleo}$ is also observed on Sulawesi. A δD_{wax} record based on alkanoic acids from Lake Towuti (Sulawesi, also at 2 °S: Konecky et al., 2016) reproduces the widely seen trend with peak Mid-Holocene precipitation and drier Late and Early Holocene, and precipitation peaks at ~3.4 ka, similar to our record and later than nearby speleothems (Konecky et al., 2016; Krause et al., 2019; Partin et al., 2007; Yuan et al., 2023). Likewise, a δD_{wax} reconstruction from a marine core off Sulawesi showed peak precipitation between 6 and 3 cal ka BP (Wicaksono et al., 2017), similar to the period of increased convection indicated in our record. The interpretation of the Sulawesi δD_{wax} appears complex, however, based on a recent C_{31} *n*-alkane δD record also from Tuwoti (Parish et al., 2024). Parish et al.'s (2024) record suggests peaking precipitation around 4 cal ka BP, as well as around 8 cal ka BP, much earlier than the record based on alkanoic acids (Konecky et al., 2016). Support for a later peak in precipitation compared to what is indicated from $\delta^{18}O_{speleo}$ is also indicated from a compilation of Holocene $\delta^{18}O$ from seawater in the IPWP, interpreted as annually averaged convection and precipitation. The seawater $\delta^{18}O$ compilation also indicates a later peak in precipitation (3–4 cal ka BP: Dang et al., 2020) in agreement with our Sumatran δD_{terr} record and the other δDwax records in the region.

The $\delta^{18}O_{speleo}$ on Borneo Gunung Buda (Partin et al., 2007) indicates that peak precipitation took place between around 4.5–4 ka, which is more similar but still earlier than our record, and later than the other speleothem records in the region. Borneo has the lowest precipitation seasonality in the region in the current climate (Supplementary Fig. 7) and on last deglaciation-timescales (Hällberg et al., 2022), and this lower seasonality may explain a lower seasonal effect on the speleothem growth and isotopic signal, in agreement with dripwater monitoring on Borneo (Ellis et al., 2020). In summary, it seems that at least some speleothem records in the IPWP may be more biased towards the rainy season than δD_{wax} records than previously established. Therefore, the new data presented here may shed additional light on how to interpret tropical speleothem records, in particular over the Holocene.

The Holocene seasonality shift may also have impacted the $\delta^{18}O$ and δD of precipitation via source changes, similar to what Konecky et al. (2016) observed for Sulawesi during the LGM. Spring rainfall moisture in Sumatra is mostly sourced from the local (short transport) Indian Ocean, while autumn precipitation has a higher proportion of moisture sourced from distal sources (long transport) from the Indian Ocean, and Java Sea (Wurtzel et al., 2018). This likely led to higher values of $\delta^{18}O$ and δD during spring and lower values during autumn via the 'source effect' (Lachniet, 2009), which may partly explain the large difference between δD_{terr} and δD_{C19}, but we are not able to constrain the extent of this effect with the data available here. Future research may explore such potential effects using isotope enabled climate model simulations, air parcel trajectory analyses and rainwater isotopic measurements, as well as carbonate and biomarker isotope measurements during different seasons.

5. Conclusions

We reconstructed a wet season δD signal from an algal lipid, and a more annually integrated δD signal from terrestrial plants. Our results show that annual precipitation peaked in Sumatra between 3 and 4.5, with a relatively dry period 8–4.5 cal ka BP, and rapid drying in the Late Holocene from ~2.8 cal ka BP. The disentangled wet season signal indicates an intensified seasonal cycle between 8 and 4.2 cal ka BP compared to the Late Holocene. The seasonality was mainly driven by seasonal insolation (precession), based on climate model simulation data from MPI-ESM1.2. Maximum orbital insolation in the boreal autumn and lowered spring insolation caused higher seasonality in the Mid-Holocene. As a result, the peatland experienced an enhanced wet period and an extended dry period relative to today. Furthermore, a period of alternating floodings, droughts and wildfires on the peatland occurred between 6 and 4.2 ka. Notably, this period of very high seasonality occurs at the same time as the collapse of a vegetated Green Sahara, hinting at tropical teleconnection that affected both regions simultaneously, likely tied to changes in the Walker Circulation.

Our multi-proxy deconvolution of annual and seasonal precipitation proxies shows that the highest amount of annual precipitation occurred around 4 cal ka BP, about 1500–2000 years later than indicated by a previous speleothem $\delta^{18}O$ reconstruction from the nearby Tangga cave. Instead, our data indicate that the speleothem $\delta^{18}O$ reflects a seasonally biased 'monsoon' signal, more similar to what is recorded by our algal δD reconstruction.

Our findings underscore the importance of seasonality in isotopic rainfall proxies. We suggest that leaf wax and algal δD records provide a useful complement to speleothem $\delta^{18}O$ studies from the same location in order to disentangle precipitation seasonality and total precipitation. The contrasting results between our δD_{C19} and δD_{terr} highlight the need to thoroughly explore the δD signal of all *n*-alkane chain lengths measured, including C_{17} and C_{19} where possible, which is rarely done in the literature. Importantly, our study clearly shows that the δD records from various organic matter sources of a certain site archive different information, which allows more detailed insight into the various aspects of hydroclimate variability than can be gained from a single proxy. Future research may further improve source constraints and understanding of δD_{wax} by analyzing the *n*-alkane distributions of modern plants in the tropics, determining the seasonality of leaf wax production and its relationship to the isotopic composition of rainfall.

Author contributions

Petter L. Hällberg: Conceptualization, Methodology, Investigation, Writing – original draft, Writing – review & editing, Visualization, Supervision of GJ. Malin E. Kylander: Supervision, Writing – review & editing. Frederik Schenk: Supervision, Writing – review & editing. Anggi Hapsari: formal analysis. Jenny K. Sjöström: Formal analysis, review and

editing. Guillermo Jarne-Bueno: Investigation, sample workup, instrument work, Formal analysis. Kweku Yamoah: discussions, Writing – review & editing. Hamdi Rifai: Resources. Rienk Smittenberg: Supervision, Funding acquisition, Formal analysis. Writing – review & editing. Nina Davtian and Joan Villanueva: Formal analysis. All authors: feedback on the manuscript and actively participated in discussions of ideas.

Declaration of competing interest

The authors declare that they have no known competing financial interests or personal relationships that could have appeared to influence the work reported in this paper.

Data availability

All geochemical data used in this manuscript can be downloaded from the Bolin Centre for Climate Research Database. Alkane, levoglucosan, mannosan and galactosan data as well as CN data is available at https://doi.org/10.17043/hallberg-2024-sumatra-1. The GDGT dataset first published in Hällberg et al. (2023) is accessible via https://bolin.su.se/data/hallberg-2022-sumatra-3. The isotopic composition of rainfall presented in Fig. 1b (Kurita et al., 2009) was kindly provided by Prof. Dr. Kurita upon personal communication and can be provided upon request from the corresponding author. Simulations from MPI-ESM can be provided by Johann Jungclaus or Bader et al. (2020).

Acknowledgements

This research was funded by the Swedish Research Council 2017–04430 to RS. Bolin Center for Climate Research funded PH's field grant to Asia. For laboratory assistance, we thank Negar Haghipour (Laboratory for Ion Beam Physics, ETH Zurich, ^{14}C analysis), Madalina Jäggi (Geological Institute, ETH Zurich, bulk EA-IRMS) and especially Julia Steinbach (Stockholm University, Dept of Geological Sciences). FS received funding from the Swedish Research Council for Sustainable Development (FORMAS 2020-01000; 2023-01631). Caroline Bouvet de la Maisonneuve at the Nanyang Technological Institute, Singapore, is thanked for organizing field work and sharing core material. The MPI-ESM model data was kindly provided by Johann Jungclaus (MPI Hamburg) and analyzed using resources provided by the National Academic Infrastructure for Supercomputing in Sweden (NAISS) and the Swedish National Infrastructure for Computing (SNIC) at Linköping University, Sweden, partially funded by the Swedish Research Council through grant agreements no. 2022–06725 and no. 2018–05973. JS was funded by Vetenskapsrådet (the Swedish Research Council, grant number 2019-03434) and Formas (Research Council for Sustainable Development, Sweden, grant number 2020-01536).

Appendix A. Supplementary data

Supplementary data to this article can be found online at https://doi.org/10.1016/j.quascirev.2024.108948.

References

Aichner, B., Herzschuh, U., Wilkes, H., 2010. Influence of aquatic macrophytes on the stable carbon isotopic signatures of sedimentary organic matter in lakes on the Tibetan Plateau. Org. Geochem. 41, 706–718. https://doi.org/10.1016/j.orggeochem.2010.02.002.

Ayliffe, L., Gagan, M., Zhao, Jx., et al., 2013. Rapid interhemispheric climate links *via* the Australasian monsoon during the last deglaciation. Nat Commun 4, 2908. https://doi.org/10.1038/ncomms3908.

Bader, J., Jungclaus, J., Krivova, N., Lorenz, S., Maycock, A., Raddatz, T., Schmidt, H., Toohey, M., Wu, C.-J., Claussen, M., 2020. Global temperature modes shed light on the Holocene temperature conundrum. Nat. Commun. 11, 4726. https://doi.org/10.1038/s41467-020-18478-6.

Baker, A., Hartmann, A., Duan, W., Hankin, S., Comas-Bru, L., Cuthbert, M.O., Treble, P. C., Banner, J., Genty, D., Baldini, L.M., Bartolomé, M., Moreno, A., Pérez-Mejías, C., Werner, M., 2019. Global analysis reveals climatic controls on the oxygen isotope composition of cave drip water. Nat. Commun. 10, 2984. https://doi.org/10.1038/s41467-019-11027-w.

Beck, H.E., Zimmermann, N.E., McVicar, T.R., Vergopolan, N., Berg, A., Wood, E.F., 2018. Present and future Köppen-Geiger climate classification maps at 1-km resolution. Sci. Data 5, 180214. https://doi.org/10.1038/sdata.2018.214.

Belgaman, H.A., Ichiyanagi, K., Suwarman, R., Tanoue, M., Aldrian, E., Utami, A.I.D., Kusumaningtyas, S.D.A., 2017. Characteristics of seasonal precipitation isotope variability in Indonesia. Hydrol. Res. Lett. 11, 92–98. https://doi.org/10.3178/hrl.11.92.

Blaauw, M., Christen, J.A., 2011. Flexible paleoclimate age-depth models using an autoregressive gamma process. Bayesian Analysis 6, 457–474. https://doi.org/10.1214/ba/1339616472.

Buckingham, F.L., Carolin, S.A., Partin, J.W., Adkins, J.F., Cobb, K.M., Day, C.C., et al., 2022. Termination 1 millennial-scale rainfall events over the Sunda Shelf. Geophysical Research Letters 49, e2021GL096937. https://dx.doi.org/10.1029/2021GL096937.

Bush, R.T., McInerney, F.A., 2013. Leaf wax n-alkane distributions in and across modern plants: implications for paleoecology and chemotaxonomy. Geochim. Cosmochim. Acta 117, 161–179. https://doi.org/10.1016/j.gca.2013.04.016.

Carré, M., Braconnot, P., Elliot, M., d'Agostino, R., Schurer, A., Shi, X., Marti, O., Lohmann, G., Jungclaus, J., Cheddadi, R., Abdelkader di Carlo, I., Cardich, J., Ochoa, D., Salas Gismondi, R., Pérez, A., Romero, P.E., Turcq, B., Corrège, T., Harrison, S.P., 2021. High-resolution marine data and transient simulations support orbital forcing of ENSO amplitude since the mid-Holocene. Quat. Sci. Rev. 268, 107125 https://doi.org/10.1016/j.quascirev.2021.107125.

Chawchai, S., Tan, L., Löwemark, L., Wang, H.-C., Yu, T.-L., Chung, Y.-C., Mii, H.-S., Liu, G., Blaauw, M., Gong, S.-Y., Wohlfarth, B., Shen, C.-C., 2021. Hydroclimate variability of central Indo-Pacific region during the Holocene. Quat. Sci. Rev. 253, 106779 https://doi.org/10.1016/j.quascirev.2020.106779.

Chen, S., Hoffmann, S.S., Lund, D.C., Cobb, K.M., Emile-Geay, J., Adkins, J.F., 2016. A high-resolution speleothem record of western equatorial Pacific rainfall: implications for Holocene ENSO evolution. Earth Planet Sci. Lett. 442, 61–71. https://doi.org/10.1016/j.epsl.2016.02.050.

Clark, I.D., Fritz, P., 1997. Environmental Isotopes in Hydrogeology. CRC Press/Lewis Publishers, Boca Raton, FL.

Cobb, K.M., Adkins, J.F., Partin, J.W., Clark, B., 2007. Regional-scale climate influences on temporal variations of rainwater and cave dripwater oxygen isotopes in northern Borneo. Earth Planet Sci. Lett. 263, 207–220. https://doi.org/10.1016/j.epsl.2007.08.024.

Cranwell, P.A., Eglinton, G., Robinson, N., 1987. Lipids of aquatic organisms as potential contributors to lacustrine sediments - ll. Org. Geochem. 11, 513–527.

Dahl, M., Gullström, M., Bernabeu, I., Serrano, O., Leiva-Dueñas, C., Linderholm, H.W., Asplund, M.E., Björk, M., Ou, T., Svensson, J.R., Andrén, E., Andrén, T., Bergman, S., Braun, S., Eklöf, A., Ežerinskis, Z., Garbaras, A., Hällberg, P., Löfgren, E., Kylander, M.E., Masqué, P., Šapolaitė, J., Smittenberg, R., Mateo, M.A., 2024. A 2,000-Year Record of Eelgrass (Zostera marina L.) Colonization Shows Substantial Gains in Blue Carbon Storage and Nutrient Retention. Glob. Biogeochem. Cycles 38, e2023GB008039. https://doi.org/10.1029/2023GB008039.

Dallmeyer, A., Claussen, M., Lorenz, S.J., Sigl, M., Toohey, M., Herzschuh, U., 2021. Holocene vegetation transitions and their climatic drivers in MPI-ESM1.2. Clim. Past 17, 2481–2513. https://doi.org/10.5194/cp-17-2481-2021.

Dang, H., Jian, Z., Wang, Y., Mohtadi, M., Rosenthal, Y., Ye, L., Bassinot, F., Kuhnt, W., 2020. Pacific warm pool subsurface heat sequestration modulated Walker circulation and ENSO activity during the Holocene. Sci. Adv. 6, eabc0402 https://doi.org/10.1126/sciadv.abc0402.

Dansgaard, W., 1964. Stable isotopes in precipitation. Tellus 16, 436–468. https://doi.org/10.1111/j.2153-3490.1964.tb00181.x.

Davtian, N., Penalva, N., Rosell-Melé, A., Villanueva, J., 2023. Selective extraction of levoglucosan and its isomers from complex matrices using ligand exchange-solid phase extraction for analysis by liquid chromatography-electrospray ionization-tandem mass spectrometry. J. Chromatogr. A 1695, 463935. https://doi.org/10.1016/j.chroma.2023.463935.

De Deckker, P., 2016. The Indo-Pacific Warm Pool: critical to world oceanography and world climate. Geosci. Lett. 3, 20. https://doi.org/10.1186/s40562-016-0054-3.

De Jonge, C., Guo, J., Hällberg, P., Griepentrog, M., Rifai, H., Richter, A., Ramirez, E., Zhang, X., Smittenberg, R.H., Peterse, F., Boeckx, P., Dercon, G., 2024. The impact of soil chemistry, moisture and temperature on branched and isoprenoid GDGTs in soils: a study using six globally distributed elevation transects. Org. Geochem. 187, 104706 https://doi.org/10.1016/j.orggeochem.2023.104706.

De Jonge, C., Hopmans, E.C., Zell, C.I., Kim, J.-H., Schouten, S., Sinninghe Damsté, J.S., 2014. Occurrence and abundance of 6-methyl branched glycerol dialkyl glycerol tetraethers in soils: implications for palaeoclimate reconstruction. Geochimica et Cosmochimica Acta 141, 97–112. https://doi.org/10.1016/j.gca.2014.06.013.

Denniston, R.F., Wyrwoll, K.-H., Asmerom, Y., Polyak, V.J., Humphreys, W.F., Cugley, J., Woods, D., LaPointe, Z., Peota, J., Greaves, E., 2013. North Atlantic forcing of millennial-scale Indo-Australian monsoon dynamics during the Last Glacial period. Quat. Sci. Rev. 72, 159–168. https://doi.org/10.1016/j.quascirev.2013.04.012.

Diefendorf, A.F., Freimuth, E.J., 2017. Extracting the most from terrestrial plant-derived n-alkyl lipids and their carbon isotopes from the sedimentary record: a review. Org. Geochem. 103, 1–21. https://doi.org/10.1016/j.orggeochem.2016.10.016.

Djamil, Y.S., Yuan, S., Lestari, R.K., Wang, X., 2023. Mechanisms and impacts of enhanced rainfall over large islands in the Maritime Continent during the mid-holocene. Clim. Dyn. https://doi.org/10.1007/s00382-023-06948-8.

Ellis, S.A., Cobb, K.M., Moerman, J.W., Partin, J.W., Bennett, A.L., Malang, J., Gerstner, H., Tuen, A.A., 2020. Extended cave drip water time series captures the

2015–2016 El Niño in northern Borneo. Geophys. Res. Lett. 47, e2019GL086363 https://doi.org/10.1029/2019GL086363.
Emile-Geay, J., Cobb, K.M., Carré, M., Braconnot, P., Leloup, J., Zhou, Y., Harrison, S.P., Corrège, T., McGregor, H.V., Collins, M., Driscoll, R., Elliot, M., Schneider, B., Tudhope, A., 2016. Links between tropical Pacific seasonal, interannual and orbital variability during the Holocene. Nat. Geosci. 9, 168–173. https://doi.org/10.1038/ngeo2608.
Fairchild, I., McMillan, E., 2007. Speleothems as indicators of wet and dry periods. Int. J. Speleol. 36, 69–74. https://doi.org/10.5038/1827-806X.36.2.2.
Feakins, S.J., Bentley, L.P., Salinas, N., Shenkin, A., Blonder, B., Goldsmith, G.R., Ponton, C., Arvin, L.J., Wu, M.S., Peters, T., West, A.J., Martin, R.E., Enquist, B.J., Asner, G.P., Malhi, Y., 2016. Plant leaf wax biomarkers capture gradients in hydrogen isotopes of precipitation from the Andes and Amazon. Geochim. Cosmochim. Acta 182, 155–172. https://doi.org/10.1016/j.gca.2016.03.018.
Ficken, K.J., Li, B., Swain, D.L., Eglinton, G., 2000. An n-alkane proxy for the sedimentary input of submerged/ oating freshwater aquatic macrophytes. Org. Geochem. 5.
Griepentrog, M., De Wispelaere, L., Bauters, M., Bodé, S., Hemp, A., Verschuren, D., Boeckx, P., 2019. Influence of plant growth form, habitat and season on leaf-wax n-alkane hydrogen-isotopic signatures in equatorial East Africa. Geochim. Cosmochim. Acta 263, 122–139. https://doi.org/10.1016/j.gca.2019.08.004.
Griffiths, M.L., Drysdale, R.N., Gagan, M.K., Zhao, J., Hellstrom, J.C., Ayliffe, L.K., Hantoro, W.S., 2013. Abrupt increase in east Indonesian rainfall from flooding of the Sunda Shelf ~9500 years ago. Quat. Sci. Rev. 74, 273–279. https://doi.org/10.1016/j.quascirev.2012.07.006.
Griffiths, M.L., Johnson, K.R., Pausata, F.S.R., White, J.C., Henderson, G.M., Wood, C.T., Yang, H., Ersek, V., Conrad, C., Sekhon, N., 2020. End of green Sahara amplified mid- to late holocene megadroughts in mainland southeast Asia. Nat. Commun. 11, 4204. https://doi.org/10.1038/s41467-020-17927-6.
Hällberg, P.L., Schenk, F., Jarne-Bueno, G., Schankat, Y., Zhang, Q., Rifai, H., Phua, M., Smittenberg, R.H., 2023. Branched GDGT source shift identification allows improved reconstruction of an 8,000-year warming trend on Sumatra. Org. Geochem. 186, 104702 https://doi.org/10.1016/j.orggeochem.2023.104702.
Hällberg, P.L., Schenk, F., Yamoah, K.A., Kuang, X., Smittenberg, R.H., 2022. Seasonal aridity in the indo-pacific warm pool during the late glacial driven by El niño-like conditions. Clim. Past 18, 1655–1674. https://doi.org/10.5194/cp-18-1655-2022.
Han, J., McCarthy, E.D., Hoeven, W.V., Calvin, M., Bradley, W.H., 1967. Organic geochemical studies, II. A preliminary report on the distribution of aliphatic hydrocarbons in algae, in bacteria, and in a recent lake sediment. Proc. Natl. Acad. Sci. 59, 29–33. https://doi.org/10.1073/pnas.59.1.29.
He, 2011. Simulating transient climate evolution of the last deglaciation with CCSM 3. PhD Thesis, University of Wisconsin-Madison.
Hersbach, H., Bell, B., Berrisford, P., Hirahara, S., Horányi, A., Muñoz-Sabater, J., Nicolas, J., Peubey, C., Radu, R., Schepers, D., Simmons, A., Soci, C., Abdalla, S., Abellan, X., Balsamo, G., Bechtold, P., Biavati, G., Bidlot, J., Bonavita, M., Chiara, G., Dahlgren, P., Dee, D., Diamantakis, M., Dragani, R., Flemming, J., Forbes, R., Fuentes, M., Geer, A., Haimberger, L., Healy, S., Hogan, R.J., Hólm, E., Janisková, M., Keeley, S., Laloyaux, P., Lopez, P., Lupu, C., Radnoti, G., Rosnay, P., Rozum, I., Vamborg, F., Villaume, S., Thépaut, J., 2020. The ERA5 global reanalysis. Q. J. R. Meteorol. Soc. 146, 1999–2049. https://doi.org/10.1002/qj.3803.
Hogg, A.G., Heaton, T.J., Hua, Q., Palmer, J.G., Turney, C.S., Southon, J., Bayliss, A., Blackwell, P.G., Boswijk, G., Bronk Ramsey, C., Pearson, C., Petchey, F., Reimer, P., Reimer, R., Wacker, L., 2020. SHCal20 southern hemisphere calibration, 0–55,000 Years cal BP. Radiocarbon 62, 759–778. https://doi.org/10.1017/RDC.2020.59.
Hopmans, E.C., Schouten, S., Sinninghe Damsté, J.S., 2016. The effect of improved chromatography on GDGT-based palaeoproxies. Organic Geochemistry 93, 1–6. https://doi.org/10.1016/j.orggeochem.2015.12.006.
Jiménez-Iñiguez, A., Ampuero, A., Valencia, B.G., Mayta, V.C., Cruz, F.W., Vuille, M., Novello, V.F., Misailidis Stríkis, N., Aranda, N., Conicelli, B., 2022. Stable isotope variability of precipitation and cave drip-water at Jumandy cave, western Amazon River basin (Ecuador). J. Hydrol. 610, 127848 https://doi.org/10.1016/j.jhydrol.2022.127848.
JMP, 2021. Version 16.1. SAS Institute Inc, Cary, NC.
Johnson, K., Hu, C., Belshaw, N., Henderson, G., 2006. Seasonal trace-element and stable-isotope variations in a Chinese speleothem: The potential for high-resolution paleomonsoon reconstruction. Earth Planet. Sci. Lett. 244, 394–407. https://doi.org/10.1016/j.epsl.2006.01.064.
Kaboth-Bahr, S., Bahr, A., Zeeden, C., Yamoah, K.A., Lone, M.A., Chuang, C.-K., Löwemark, L., Wei, K.-Y., 2021. A tale of shifting relations: east Asian summer and winter monsoon variability during the Holocene. Sci. Rep. 11, 6938. https://doi.org/10.1038/s41598-021-85444-7.
Katrantsiotis, C., Norström, E., Smittenberg, R.H., Salonen, J.S., Plikk, A., Helmens, K., 2021. Seasonal variability in temperature trends and atmospheric circulation systems during the Eemian (Last Interglacial) based on n-alkanes hydrogen isotopes from Northern Finland. Quat. Sci. Rev. 273, 107250 https://doi.org/10.1016/j.quascirev.2021.107250.
Konecky, B., Russell, J., Bijaksana, S., 2016. Glacial aridity in central Indonesia coeval with intensified monsoon circulation. Earth Planet Sci. Lett. 437, 15–24. https://doi.org/10.1016/j.epsl.2015.12.037.
Krause, C.E., Gagan, M.K., Dunbar, G.B., Hantoro, W.S., Hellstrom, J.C., Cheng, H., Edwards, R.L., Suwargadi, B.W., Abram, N.J., Rifai, H., 2019. Spatio-temporal evolution of Australasian monsoon hydroclimate over the last 40,000 years. Earth Planet Sci. Lett. 513, 103–112. https://doi.org/10.1016/j.epsl.2019.01.045.
Kurita, N., Ichiyanagi, K., Matsumoto, J., Yamanaka, M.D., Ohata, T., 2009. The relationship between the isotopic content of precipitation and the precipitation amount in tropical regions. J. Geochem. Explor. 102, 113–122. https://doi.org/10.1016/j.gexplo.2009.03.002.
Lachniet, M.S., 2009. Climatic and environmental controls on speleothem oxygen-isotope values. Quat. Sci. Rev. 28, 412–432. https://doi.org/10.1016/j.quascirev.2008.10.021.
Lases-Hernandez, F., Medina-Elizalde, M., Burns, S., DeCesare, M., 2019. Long-term monitoring of drip water and groundwater stable isotopic variability in the Yucatán Peninsula: implications for recharge and speleothem rainfall reconstruction. Geochim. Cosmochim. Acta 246, 41–59. https://doi.org/10.1016/j.gca.2018.11.028.
Laskar, J., Robutel, P., Joutel, F., Gastineau, M., Correia, A.C.M., Levrard, B., 2004. A long-term numerical solution for the insolation quantities of the Earth. Astron. Astrophys. 428, 261–285. https://doi.org/10.1051/0004-6361:20041335.
Liu, Z., Zhang, X., Xiao, Z., He, X., Rao, Z., Guan, H., 2023. The relations between summer droughts/floods and oxygen isotope composition of precipitation in the Dongting Lake basin. Int. J. Climatol. 43, 3590–3604. https://doi.org/10.1002/joc.8047.
Malhi, Y., Farfán Amézquita, F., Doughty, C.E., Silva-Espejo, J.E., Girardin, C.A.J., Metcalfe, D.B., Aragão, L.E.O.C., Huaraca-Quispe, L.P., Alzamora-Taype, I., Eguiluz-Mora, L., Marthews, T.R., Halladay, K., Quesada, C.A., Robertson, A.L., Fisher, J.B., Zaragoza-Castells, J., Rojas-Villagra, C.M., Pelaez-Tapia, Y., Salinas, N., Meir, P., Phillips, O.L., 2014a. The productivity, metabolism and carbon cycle of two lowland tropical forest plots in south-western Amazonia, Peru. Plant Ecol. Divers. 7, 85–105. https://doi.org/10.1080/17550874.2013.820805.
Malhi, Y., Gardner, T.A., Goldsmith, G.R., Silman, M.R., Zelazowski, P., 2014b. Tropical forests in the anthropocene. Annu. Rev. Environ. Resour. 39, 125–159. https://doi.org/10.1146/annurev-environ-030713-155141.
Marynowski, L., Simoneit, B.R.T., 2022. Saccharides in atmospheric particulate and sedimentary organic matter: status overview and future perspectives. Chemosphere 288, 132376. https://doi.org/10.1016/j.chemosphere.2021.132376.
Moerman, J.W., Cobb, K.M., Adkins, J.F., Sodemann, H., Clark, B., Tuen, A.A., 2013. Diurnal to interannual rainfall δ18O variations in northern Borneo driven by regional hydrology. Earth Planet Sci. Lett. 369–370, 108–119. https://doi.org/10.1016/j.epsl.2013.03.014.
Moerman, J.W., Cobb, K.M., Partin, J.W., Meckler, A.N., Carolin, S.A., Adkins, J.F., Lejau, S., Malang, J., Clark, B., Tuen, A.A., 2014. Transformation of ENSO-related rainwater to dripwater δ18O variability by vadose water mixing. Geophys. Res. Lett. 41, 7907–7915. https://doi.org/10.1002/2014GL061696.
Mohtadi, M., Prange, M., Steinke, S., 2016. Palaeoclimatic insights into forcing and response of monsoon rainfall. Nature 533, 191–199. https://doi.org/10.1038/nature17450.
Morley, R.J., 1982. A palaeoecological interpretation of a 10,000 Year pollen record from danau Padang, central Sumatra, Indonesia. J. Biogeogr. 9, 151. https://doi.org/10.2307/2844699.
Muschitiello, F., Pausata, F.S.R., Watson, J.E., Smittenberg, R.H., Salih, A.A.M., Brooks, S.J., Whitehouse, N.J., Karlatou-Charalampopoulou, A., Wohlfarth, B., 2015. Fennoscandian freshwater control on Greenland hydroclimate shifts at the onset of the Younger Dryas. Nat. Commun. 6, 8939. https://doi.org/10.1038/ncomms9939.
Niedermeyer, E.M., Sessions, A.L., Feakins, S.J., Mohtadi, M., 2014. Hydroclimate of the western indo-pacific warm pool during the past 24,000 years. Proc. Natl. Acad. Sci. 111, 9402–9406. https://doi.org/10.1073/pnas.1323585111.
Norström, E., Norén, G., Smittenberg, R.H., Massuanganhe, E.A., Ekblom, A., 2018. Leaf wax δD inferring variable medieval hydroclimate and early initiation of Little Ice Age (LIA) dryness in southern Mozambique. Glob. Planet. Change 170, 221–233. https://doi.org/10.1016/j.gloplacha.2018.09.004.
Norström, E., West, J., Kouli, K., Katrantsiotis, C., Hättestrand, M., Smittenberg, R.H., 2021. Evaluation of anhydrosugars as a molecular proxy for paleofire activity: a case study on a Holocene sediment core from Agios Floros, Peloponnese, Greece. Org. Geochem. 153, 104193 https://doi.org/10.1016/j.orggeochem.2021.104193.
Pang, Y., Zhou, B., Ma, C., Jiang, J., Taylor, D., Lu, Y., 2022. Alkane variation in peat reveals palaeohydrological changes since the Little Ice Age in eastern China. Palaeogeogr. Palaeoclimatol. Palaeoecol. 585, 110727. https://doi.org/10.1016/j.palaeo.2021.110727.
Parish, M., Russell, J., Konecky, B., Du, X., He, C., Bijaksana, S., Vogel, H., 2024. Changes in Indo-Pacific Warm Pool hydroclimate and vegetation during the last deglaciation. Quat. Sci. Rev. 336, 108755 https://doi.org/10.1016/j.quascirev.2024.108755.
Partin, J.W., Cobb, K.M., Adkins, J.F., Clark, B., Fernandez, D.P., 2007. Millennial-scale trends in west Pacific warm pool hydrology since the Last Glacial Maximum. Nature 449, 452–455. https://doi.org/10.1038/nature06164.
Patterson, E.W., Johnson, K.R., Griffiths, M.L., Kinsley, C.W., McGee, D., Du, X., Pico, T., Wolf, A., Ersek, V., Mortlock, R.A., Yamoah, K.A., Bùi, T.N., Trần, M.X., Đỗ-Trọng, Q., Võ, T.V., Đinh, T.H., 2023. Glacial changes in sea level modulated millennial-scale variability of Southeast Asian autumn monsoon rainfall. Proc. Natl. Acad. Sci. 120, e2219489120 https://doi.org/10.1073/pnas.2219489120.
Qiu, W., Yang, Y., Jiang, X., Wang, X., Wang, Y., Cai, J., Liao, Y., Feng, T., Gao, K., Zhai, S., 2023. Oxygen isotope variability in precipitation, dripwater, and modern calcite responding to ENSO based on 11 years' monitoring in Yuhua Cave, Southeast China. J. Hydrol. 624, 129937 https://doi.org/10.1016/j.jhydrol.2023.129937.
Rach, O., Brauer, A., Wilkes, H., Sachse, D., 2014. Delayed hydrological response to Greenland cooling at the onset of the Younger Dryas in western Europe. Nat. Geosci. 7, 109–112. https://doi.org/10.1038/ngeo2053.
Ridley, H., Baldini, J., Prufer, K., Walczak, I., Breitenbach, S., 2015. High-resolution monitoring of Yok Balum Cave, Belize: an investigation of seasonal ventilation regimes and the atmospheric and drip-flow response to a local earthquake. J. Cave Karst Stud. 77, 183–199. https://doi.org/10.4311/2014ES0117.

Rozanski, K., Araguás-Araguás, L., Gonfiantini, R., 2013. Isotopic patterns in modern global precipitation. In: Swart, P.K., Lohmann, K.C., Mckenzie, J., Savin, S. (Eds.), Geophysical Monograph Series. American Geophysical Union, pp. 1–36. https://doi.org/10.1029/GM078p0001. Washington, D. C.

Sachse, D., Billault, I., Bowen, G.J., Chikaraishi, Y., Dawson, T.E., Feakins, S.J., Freeman, K.H., Magill, C.R., McInerney, F.A., van der Meer, M.T.J., Polissar, P., Robins, R.J., Sachs, J.P., Schmidt, H.-L., Sessions, A.L., White, J.W.C., West, J.B., Kahmen, A., 2012. Molecular paleohydrology: interpreting the hydrogen-isotopic composition of lipid biomarkers from photosynthesizing organisms. Annu. Rev. Earth Planet Sci. 40, 221–249. https://doi.org/10.1146/annurev-earth-042711-105535.

Sachse, D., Dawson, T.E., Kahmen, A., 2015. Seasonal variation of leaf wax *n* -alkane production and δ^{2} H values from the evergreen oak tree, *Quercus agrifolia*. Isotopes Environ. Health Stud. 51, 124–142. https://doi.org/10.1080/10256016.2015.1011636.

Sachse, D., Radke, J., Gleixner, G., 2004. Hydrogen isotope ratios of recent lacustrine sedimentary n-alkanes record modern climate variability. Geochim. Cosmochim. Acta 68, 4877–4889. https://doi.org/10.1016/j.gca.2004.06.004.

Steinke, S., Mohtadi, M., Prange, M., Varma, V., Pittauerova, D., Fischer, H.W., 2014. Mid- to Late-Holocene Australian–Indonesian summer monsoon variability. Quat. Sci. Rev. 93, 142–154. https://doi.org/10.1016/j.quascirev.2014.04.006.

Suciu, L.G., Masiello, C.A., Griffin, R.J., 2019. Anhydrosugars as tracers in the Earth system. Biogeochemistry 146, 209–256. https://doi.org/10.1007/s10533-019-00622-0.

Theaker, C.M., Carolin, S.A., Day, C.C., Cobb, K.M., Chen, S., Grothe, P.R., Couper, H.O., 2024. Borneo stalagmite evidence of significantly reduced El niño-southern oscillation variability at 4.1 kyBP. Geophys. Res. Lett. 51, e2023GL107111 https://doi.org/10.1029/2023GL107111.

Thomas, E.K., Hollister, K.V., Cluett, A.A., Corcoran, M.C., 2020. Reconstructing arctic precipitation seasonality using aquatic leaf wax δ^{2} H in lakes with contrasting residence times. Paleoceanogr. Paleoclimatology 35, e2020PA003886. https://doi.org/10.1029/2020PA003886.

Tian, Y., Fleitmann, D., Zhang, Q., Sha, L., Wassenburg, JasperA., Axelsson, J., Zhang, H., Li, X., Hu, J., Li, H., Zhao, L., Cai, Y., Ning, Y., Cheng, H., 2023. Holocene climate change in southern Oman deciphered by speleothem records and climate model simulations. Nat. Commun. 14, 4718. https://doi.org/10.1038/s41467-023-40454-z.

Wicaksono, S.A., Russell, J.M., Holbourn, A., Kuhnt, W., 2017. Hydrological and vegetation shifts in the wallacean region of central Indonesia since the last glacial maximum. Quat. Sci. Rev. 157, 152–163. https://doi.org/10.1016/j.quascirev.2016.12.006.

Wolf, A., Ersek, V., Braun, T., French, A.D., McGee, D., Bernasconi, S.M., Skiba, V., Griffiths, M.L., Johnson, K.R., Fohlmeister, J., Breitenbach, S.F.M., Pausata, F.S.R., Tabor, C.R., Longman, J., Roberts, W.H.G., Chandan, D., Peltier, W.R., Salzmann, U., Limbert, D., Trinh, H.Q., Trinh, A.D., 2023. Deciphering local and regional hydroclimate resolves contradicting evidence on the Asian monsoon evolution. Nat. Commun. 14, 5697. https://doi.org/10.1038/s41467-023-41373-9.

Wolf, A., Roberts, W.H.G., Ersek, V., et al., 2020. Rainwater isotopes in central Vietnam controlled by two oceanic moisture sources and rainout effects. Sci Rep 10, 16482. https://doi.org/10.1038/s41598-020-73508-z.

Wurtzel, J.B., Abram, N.J., Lewis, S.C., Bajo, P., Hellstrom, J.C., Troitzsch, U., Heslop, D., 2018. Tropical Indo-Pacific hydroclimate response to North Atlantic forcing during the last deglaciation as recorded by a speleothem from Sumatra, Indonesia. Earth Planet Sci. Lett. 492, 264–278. https://doi.org/10.1016/j.epsl.2018.04.001.

Yamoah, K.K.A., Chabangborn, A., Chawchai, S., Väliranta, M., Wohlfarth, B., Smittenberg, R.H., 2016. Large variability in n-alkane δ13C values in Lake Pa Kho (Thailand) driven by wetland wetness and aquatic productivity. Org. Geochem. 97, 53–60. https://doi.org/10.1016/j.orggeochem.2016.04.008.

Yang, H., Xiao, W., Słowakiewicz, M., Ding, W., Ayari, A., Dang, X., Pei, H., 2019. Depth-dependent variation of archaeal ether lipids along soil and peat profiles from southern China: implications for the use of isoprenoidal GDGTs as environmental tracers. Org. Geochem. 128, 42–56. https://doi.org/10.1016/j.orggeochem.2018.12.009.

Yuan, S., Chiang, H.-W., Liu, G., Bijaksana, S., He, S., Jiang, X., Imran, A.M., Wicaksono, S.A., Wang, X., 2023. The strength, position, and width changes of the intertropical convergence zone since the Last Glacial Maximum. Proc. Natl. Acad. Sci. 120, e2217064120 https://doi.org/10.1073/pnas.2217064120.

Zhang, H., Griffiths, M.L., Chiang, J.C.H., Kong, W., Wu, S., Atwood, A., Huang, J., Cheng, H., Ning, Y., Xie, S., 2018. East Asian hydroclimate modulated by the position of the westerlies during Termination I. Science 362, 580–583. https://doi.org/10.1126/science.aat9393.

Zhang, Y., Su, Y., Yu, J., Liu, Z., Du, Y., Jin, M., 2019. Anthropogenically driven differences in n-alkane distributions of surface sediments from 19 lakes along the middle Yangtze River, Eastern China. Environ. Sci. Pollut. Res. 26, 22472–22484. https://doi.org/10.1007/s11356-019-05536-w.

Zhang, Y.G., Zhang, C.L., Liu, X.-L., Li, L., Hinrichs, K.-U., Noakes, J.E., 2011. Methane Index: a tetraether archaeal lipid biomarker indicator for detecting the instability of marine gas hydrates. Earth Planet Sci. Lett. 307, 525–534. https://doi.org/10.1016/j.epsl.2011.05.031.

Kaufman, D., McKay, N., Routson, C., Erb, M., Davis, B., Heiri, O., Jaccard, S., Tierney, J., Dätwyler, C., Axford, Y., Brussel, T., Cartapanis, O., Chase, B., Dawson, A., de Vernal, A., Engels, S., Jonkers, L., Marsicek, J., Moffa-Sánchez, P., Morrill, C., Orsi, A., Rehfeld, K., Saunders, K., Sommer, P.S., Thomas, E., Tonello, M., Tóth, M., Vachula, R., Andreev, A., Bertrand, S., Biskaborn, B., Bringué, M., Brooks, S., Caniupán, M., Chevalier, M., Cwynar, L., Emile-Geay, J., Fegyveresi, J., Feurdean, A., Finsinger, W., Fortin, M.-C., Foster, L., Fox, M., Gajewski, K., Grosjean, M., Hausmann, S., Heinrichs, M., Holmes, N., Ilyashuk, B., Ilyashuk, E., Juggins, S., Khider, D., Koinig, K., Langdon, P., Larocque-Tobler, I., Li, J., Lotter, A., Luoto, T., Mackay, A., Magyari, E., Malevich, S., Mark, B., Massaferro, J., Montade, V., Nazarova, L., Novenko, E., Pařil, P., Pearson, E., Peros, M., Pienitz, R., Póciennik, M., Porinchu, D., Potito, A., Rees, A., Reinemann, S., Roberts, S., Rolland, N., Salonen, S., Self, A., Seppä, H., Shala, S., St-Jacques, J.-M., Stenni, B., Syrykh, L., Tarrats, P., Taylor, K., van den Bos, V., Velle, G., Wahl, E., Walker, I., Wilmshurst, J., Zhang, E., Zhilich, S., 2020. A global database of Holocene paleotemperature records. Scientific Data 7, 115. https://doi.org/10.1038/s41597-020-0445-3.